

## Insights into Nitrate Reduction over Indium-Decorated Palladium Nanoparticle Catalysts

Sujin Guo, Kimberly Heck, Sashank Kasiraju, Huifeng Qian, Zhun Zhao, Lars C. Grabow, Jeff Miller, and Michael S. Wong

*ACS Catal.*, **Just Accepted Manuscript** • DOI: 10.1021/acscatal.7b01371 • Publication Date (Web): 21 Nov 2017

Downloaded from <http://pubs.acs.org> on November 21, 2017

### Just Accepted

“Just Accepted” manuscripts have been peer-reviewed and accepted for publication. They are posted online prior to technical editing, formatting for publication and author proofing. The American Chemical Society provides “Just Accepted” as a free service to the research community to expedite the dissemination of scientific material as soon as possible after acceptance. “Just Accepted” manuscripts appear in full in PDF format accompanied by an HTML abstract. “Just Accepted” manuscripts have been fully peer reviewed, but should not be considered the official version of record. They are accessible to all readers and citable by the Digital Object Identifier (DOI®). “Just Accepted” is an optional service offered to authors. Therefore, the “Just Accepted” Web site may not include all articles that will be published in the journal. After a manuscript is technically edited and formatted, it will be removed from the “Just Accepted” Web site and published as an ASAP article. Note that technical editing may introduce minor changes to the manuscript text and/or graphics which could affect content, and all legal disclaimers and ethical guidelines that apply to the journal pertain. ACS cannot be held responsible for errors or consequences arising from the use of information contained in these “Just Accepted” manuscripts.



# Insights into Nitrate Reduction over Indium-Decorated Palladium Nanoparticle Catalysts

*Sujin Guo<sup>1,2†</sup>, Kimberly Heck<sup>†3</sup>, Sashank Kasiraju<sup>4</sup>, Huifeng Qian<sup>3</sup>, Zhun Zhao<sup>3</sup>, Lars C. Grabow<sup>4\*</sup>, Jeffrey T. Miller<sup>5</sup> and Michael S. Wong<sup>1,2,3,6,7\*</sup>*

<sup>1</sup>Department of Civil & Environmental Engineering, <sup>2</sup>Nanosystems Engineering Research Center for Nanotechnology-Enabled Water Treatment, <sup>3</sup>Department of Chemical and Biomolecular Engineering, Rice University, 6100 S. Main Street, Houston, TX 77005, <sup>4</sup>Department of Chemical and Biomolecular Engineering, University of Houston, 4726 Calhoun Road, Houston, TX 77204-4004, <sup>5</sup>Department of Chemical Engineering, Purdue University, 480 Stadium Mall Drive, West Lafayette, IN 47907, <sup>6</sup>Department of Chemistry, <sup>7</sup>Department of Materials Science and NanoEngineering, Rice University, 6100 S. Main Street, Houston, TX 77005

**\*To Whom Correspondence Should Be Addressed** E-mail: mswong@rice.edu, grabow@uh.edu

<sup>†</sup> These authors contributed equally to the study

**Abstract**

Nitrate ( $\text{NO}_3^-$ ) is an ubiquitous groundwater contaminant, and is detrimental to human health. Bimetallic palladium-based catalysts have been found to be promising for treating nitrate (and nitrite,  $\text{NO}_2^-$ ) contaminated waters. Those containing indium (In) are unusually active, but the mechanistic explanation for catalyst performance remains largely unproven. We report that In deposited on Pd nanoparticles (NPs) ("In-on-Pd NPs") shows room-temperature nitrate catalytic reduction activity that varies with volcano-shape dependence on In surface coverage. The most active catalyst had an In surface coverage of 40%, with a pseudo-first order normalized rate constant of  $k_{cat} \sim 7.6 \text{ L g}_{\text{surface-metal}}^{-1} \text{ min}^{-1}$ , whereas monometallic Pd NPs and  $\text{In}_2\text{O}_3$  have nondetectible activity for nitrate reduction. X-ray absorption spectroscopy (XAS) results indicated that In is in oxidized form in the as-synthesized catalyst; it reduces to zerovalent metal in the presence of  $\text{H}_2$  and re-oxidizes following  $\text{NO}_3^-$  contact. Selectivity in excess of 95% to nontoxic  $\text{N}_2$  was observed for all the catalysts. Density functional theory (DFT) simulations suggest that submonolayer coverage amounts of metallic In provide strong binding sites for nitrate adsorption and they lower the activation barrier for the nitrate-to-nitrite reduction step. This improved understanding of the In active site expands the prospects of improved denitrification using metal-on-metal catalysts.

**Keywords:** nitrate reduction; bimetallic catalyst; DFT; indium; palladium; core-shell

## Introduction

Nitrate ( $\text{NO}_3^-$ ) is a contaminant detected globally in surface water and underground aquifers. Nitrate pollution occurs due to the overuse of nitrogen-rich agriculture fertilizers, wastewater discharge, and contaminant leaching from landfills.<sup>1-3</sup> This anion, in addition to its partially reduced form, nitrite ( $\text{NO}_2^-$ ), can cause adverse health effects in humans including methemoglobinemia (blue baby syndrome). When ingested, these compounds can be metabolized into N-nitroso compounds, which may result in cancer and hypertension.<sup>4,5</sup> Additionally, nitrate is suspected to increase cocontamination of uranium.<sup>6</sup> The United States Environmental Protection Agency (US EPA) has mandated maximum contaminant levels (MCL) of  $\text{NO}_3^-$  and  $\text{NO}_2^-$  of 10 mg-N/L (mg-nitrogen per liter of water) and 1.0 mg-N/L, respectively,<sup>7</sup> while the European Drinking Water Directive limits the concentration of  $\text{NO}_3^-$  and  $\text{NO}_2^-$  to 11.3 mg-N/L and 0.15 mg-N/L, respectively.<sup>8</sup> The limits proposed by the World Health Organization are 11.3 mg-N/L for  $\text{NO}_3^-$  and 0.91 mg-N/L for  $\text{NO}_2^-$ .<sup>9</sup>

The most widely used technologies to treat nitrate/nitrite include ion exchange, reverse osmosis and biological denitrification.<sup>2,10,11</sup> Ion exchange is used for large-scale treatment, while reverse osmosis is more suitable for smaller scale treatments. However, ion exchange and reverse osmosis processes produce concentrated nitrate/nitrite-containing waste streams that must undergo further treatment prior to disposal. Biological denitrification is sensitive to pH and the presence of other salts at the contaminated site. Moreover, long startup times and concerns regarding pathogens and active biomass during intermittent operations limit its applicability.<sup>12,13</sup>

The catalytic reduction of environmental contaminants has attracted attention as a promising solution due to their high activity and selectivity to environmentally benign products.<sup>14-16</sup> For example, monometallic and bimetallic  $\text{Pd}^{16-20}$  and  $\text{PdAu}^{20}$  catalysts have been shown to be very

1  
2  
3 active and selective to the reduction of nitrite to dinitrogen (without the formation of  $\text{NH}_3/\text{NH}_4^+$ ).  
4  
5 Pd alone has very low reduction activity for nitrate,<sup>21</sup> but its combination with certain secondary  
6  
7 metals greatly increases catalytic activity.<sup>22–27</sup> Of these catalysts, InPd bimetals are preferred  
8  
9 due to their high activity and high selectivity to dinitrogen gas over toxic ammonia.<sup>28–30</sup>  
10  
11

12 Mechanistically, it is supposed that InPd catalysts contain metallic In that oxidizes in order to  
13  
14 reduce  $\text{NO}_3^-$  to  $\text{NO}_2^-$ . The nitrite then surface diffuses to neighboring Pd sites to be further  
15  
16 reduced to  $\text{N}_2$  (or  $\text{NH}_3$ ) through a series of surface reaction steps with hydrogen adatoms formed  
17  
18 from  $\text{H}_2$  chemisorption. These H-adatoms are presumably responsible for regenerating the In  
19  
20 sites. Metal loading, atomic configuration, and metal nanoparticle size have been found to affect  
21  
22 the rate of nitrate reduction.<sup>31–34</sup> Since the first publication in 2000 by Vorlop and coworkers  
23  
24 though,<sup>28</sup> the exact nature or structure of the In active sites remains unknown.  
25  
26  
27

28 Our previous studies have focused on the synthesis of model Pd-on-Au NP catalysts to better  
29  
30 understand hydrodehalogenation reactions<sup>35–37</sup>, nitrite reduction, glycerol oxidation, and  
31  
32 nitrophenol reduction.<sup>20,38–40</sup> In this work, we deposited In on the surface of monodisperse Pd  
33  
34 NPs, so as to better control the structure of the bimetallic In-on-Pd NP catalysts. We prepared a  
35  
36 series of In-on-Pd NPs with different surface coverages of In, and quantified their reactivity for  
37  
38 nitrate reduction. By using XPS and *ex situ* and *in situ* XAS characterization techniques, we  
39  
40 identified likely catalyst surface structures, and correlated them with observed catalyst activities  
41  
42 and selectivities. We performed DFT calculations using different In-on-Pd slab models to  
43  
44 estimate the relevant adsorption and transition state energies, giving further insights about the  
45  
46 role and nature of the In surface structures.  
47  
48  
49  
50  
51  
52  
53  
54  
55  
56  
57  
58  
59  
60

## Materials and methods

### Materials

Palladium (II) acetate ( $\text{Pd}(\text{CH}_3\text{COO})_2$ , 98%), 2-ethoxyethanol ( $\text{C}_4\text{H}_{10}\text{O}_2$ , 99%), polyvinylpyrrolidone (PVP,  $M_w \sim 55,000$ ), indium chloride tetrahydrate ( $\text{InCl}_3 \cdot 4\text{H}_2\text{O}$ , 97%), sodium nitrate ( $\text{NaNO}_3$ , >99.0%), sodium nitrite ( $\text{NaNO}_2$ , >97.0%), 1 wt% Pd on  $\text{Al}_2\text{O}_3$  catalyst ( $\text{Pd}/\text{Al}_2\text{O}_3$ ) and modified Griess's reagent were purchased from Sigma-Aldrich. Hydrogen gas (99.999%), carbon dioxide gas (99.995%) and nitrogen gas (99.999%) were purchased from Matheson. All experiments were conducted using deionized (DI) water (>18  $\text{M}\Omega\text{cm}$ , Barnstead NANOpure Diamond).

### Catalyst preparation and characterization

To synthesize Pd NPs, 0.255 g PVP and 0.1332 g palladium (II) acetate were dissolved in 15 mL 2-ethoxyethanol. Before heating, the solution was purged with nitrogen gas for 15 min to remove dissolved oxygen. Using a microwave reactor (Anton-Parr Monowave 300), the brown-colored solution was heated to 120 °C and held at this temperature for 1 h. The solution was stirred at 600 rpm throughout the procedure. The color of the solution was black after heat treatment, indicative of the formation of Pd NPs from the Pd (II) precursor. The In-on-Pd bimetallic catalysts with different In surface coverages (sc%) were prepared by adding the appropriate amounts of In salt precursor to the Pd sol, and contacting with  $\text{H}_2$  gas (Table S1). The In surface coverage was calculated as the percentage of In atoms needed to fill the 10th shell around a magic cluster of 9 closed shells of Pd atoms (which approximates the 5.32 nm Pd NPs, Table S2).<sup>41</sup> Our model assumes that all the In precursor is fully reduced onto the Pd surface and that the Pd particles are monodisperse. The various surface coverage percentages (sc%) of In-on-Pd NPs were obtained by mixing 0, 0.170, 0.425, 0.511, 0.681, 0.851, 1.191, 1.872 mL  $\text{InCl}_3 \cdot 4\text{H}_2\text{O}$

1  
2  
3 solution (0.04 M) with 5 mL of the as-synthesized Pd NPs, then adding DI water to the solution  
4  
5 to reach a volume of 6.872 mL (for 0, 10, 25, 30, 40, 50, 70, and 110 sc%; see Table S3 for  
6  
7 weight fractions). The solution was stirred for 1 min and then bubbled with H<sub>2</sub> gas for 15 min at  
8  
9 a flow rate of ~200 mL min<sup>-1</sup>.

10  
11  
12 For comparison, a supported PdIn catalyst was prepared with a Pd:In weight ratio of 95:5  
13  
14 (equivalent to In-on-Pd NPs of 40 sc% In) through wet impregnation similar to that described by  
15  
16 Werth and coworkers.<sup>42</sup> 350 mg of a commercially available 1 wt% Pd/Al<sub>2</sub>O<sub>3</sub> was weighed and  
17  
18 24 μL of 0.2 M indium chloride solution was added. The resulting material was then air dried at  
19  
20 120 °C for 14 h and treated under H<sub>2</sub> gas at 120 °C for 1 h.

21  
22  
23  
24 Transmission electron microscopy (TEM) images were obtained using a JEOL 2010  
25  
26 transmission electron microscope operating at an accelerating voltage of 200 kV. The particle  
27  
28 size distribution was calculated by counting at least 200 particles with ImageJ. The X-ray  
29  
30 photoelectron spectroscopy (XPS) data was obtained by using a PHI Quantera System with  
31  
32 monochromatic Al K<sub>R</sub> radiation (1486.7 eV). XPS samples were prepared by placing a vial of 10  
33  
34 mL of catalyst in a 50°C oven overnight to evaporate solvent to form a black plate-like solid and  
35  
36 stored under atmospheric conditions at room temperature before analysis. pH measurements  
37  
38 were taken using a VWR sympHony SB20 meter with a standard pH electrode. In K (27.90 to  
39  
40 27.98 keV) edge or Pd K (24.32 to 24.40 keV) edge XAS measurements were carried out on the  
41  
42 insertion and bending magnet devices (beamline 10-ID-B and 10-BM-B) of the Materials  
43  
44 Research Collaborative Access Team (MRCAT) at the Advanced Photon Source at Argonne  
45  
46 National Laboratory. The X-ray beam was 0.5 × 0.5 mm<sup>2</sup> at the ID beamline and 0.5 × 2.0 mm<sup>2</sup> at  
47  
48 the BM beamline, and measurements were made in transmission mode with the ionization  
49  
50 chambers optimized for maximum current with linear response, and were obtained  
51  
52  
53  
54  
55  
56  
57  
58  
59  
60

1  
2  
3 simultaneously with In or Pd foil spectra for energy calibration. Samples of the In-on-Pd NPs of  
4  
5 10 sc%, 40 sc%, and 110 sc% were prepared by adding 600 mg activated carbon to 20 mL of the  
6  
7 respective In-on-Pd suspension. After stirring overnight, the carbon slurry was removed by  
8  
9 centrifugation, dried in an oven at 50°C overnight, and stored under ambient conditions. These  
10  
11 carbon-supported NPs samples were also heat-treated at 200 °C for 30 min under flowing 4% H<sub>2</sub>  
12  
13 gas. For the *in situ* experiments, solutions were prepared by bubbling DI water for 30 min to  
14  
15 saturate the water with the gas of choice (air, 4% H<sub>2</sub>, or inert N<sub>2</sub>). The *in situ* XANES were  
16  
17 obtained by loading catalyst powder into a polymer, *in situ* solution cell designed for air sensitive  
18  
19 homogeneous and slurry catalysts and is described in detail in a previous publication.<sup>43</sup> This cell  
20  
21 is equipped with inlet and outlet ports to flush the cell with the desired solution. Approximately 5  
22  
23 mL of the solution of interest (air-saturated water, 4% H<sub>2</sub>-saturated water, or 100 ppm nitrate  
24  
25 solution purged with N<sub>2</sub> gas) was flushed through the cell (with ~3 mL volume), prior to the cell  
26  
27 being sealed for XANES measurements. At the Pd and In K-edge spectra, a 1-cm path length  
28  
29 was used for *in situ* treatments.  
30  
31  
32  
33  
34

35 WINXAS 3.1 software was used to fit the XAS data. The EXAFS coordination parameters  
36  
37 were obtained by a least-squares fit in R-space of the k<sup>2</sup>-weighted Fourier transform data from  
38  
39 3.0 to 12.0 Å. The first shell fit of the magnitude and imaginary parts were performed between  
40  
41 1.6 to 2.9 Å for the Pd edge. At the In edge, the first shell fit was performed from 1.8 to 2.8 Å.  
42  
43 An average coordination number and bond distance were determined for Pd-Pd and Pd-In  
44  
45 scattering by fitting with the experimental phase shift and back scattering amplitude of Pd-Pd  
46  
47 scattering extracted from Pd foil XAS data (12 Pd-Pd at 2.75 Å). Such treatment was rationalized  
48  
49 based on the small difference in phase shift and amplitude between Pd-Pd and Pd-In scattering  
50  
51  
52  
53  
54  
55  
56  
57  
58  
59  
60

1  
2  
3 due to the close atomic number of Pd and In. Fits were performed by refinement of the  
4 coordination number (CN), bond distance (R),  $\Delta\sigma^2$ , and energy shift ( $E_0$ ).  
5  
6

### 7 **Catalyst activity characterization**

8  
9  
10 Similar to our previous experiments,<sup>44</sup> batch nitrate reduction experiments were conducted in a  
11 screw-cap bottle (125 mL, Alltech) with PTFE-sealed threads and a PTFE-silicone septum. The  
12 initial water volume was controlled so that the final liquid reaction volume was 99.5 mL after  
13 adding the catalyst NPs. The amount of In-on-Pd NPs added was chosen such that the total In  
14 amount per reaction was 0.553 mg, the final catalyst charge concentration was 5.53 mg-In L<sup>-1</sup>  
15 (Table S4). The solution was then bubbled simultaneously with H<sub>2</sub> gas (120 mL/min, to serve as  
16 reductant) and CO<sub>2</sub> gas (120 mL/min, to buffer the solution to a pH value of 4-6) for 30 min to  
17 displace dissolved oxygen and to fill the headspace with a hydrogen/CO<sub>2</sub> atmosphere (1 atm).  
18 All the catalytic reactions were conducted at room temperature (~23 °C). After hydrogen and  
19 carbon dioxide bubbling, 0.5 mL of NaNO<sub>3</sub> solution (10 mg/mL) was injected into the sealed  
20 bottle to start the reaction (initial NO<sub>3</sub><sup>-</sup> concentration was 50 mg NO<sub>3</sub><sup>-</sup> per L). The reaction was  
21 monitored periodically by withdrawing 2 mL aliquots from the reactor. The In-on-Pd NPs  
22 showed negligible UV-vis absorbance, so no separation of the particles from the reaction  
23 medium was performed prior to UV-vis spectroscopy measurements.  
24  
25  
26  
27  
28  
29  
30  
31  
32  
33  
34  
35  
36  
37  
38  
39  
40  
41

42 The activity of the supported catalysts was tested similarly, except that the solid catalyst was  
43 added directly to the reactor before the H<sub>2</sub>/CO<sub>2</sub> bubbling (see Table S5 for catalyst loading). As a  
44 control, experiments using 3.51 mg (1.15 mL of 3.05 mg Pd/mL solution) of monometallic Pd  
45 NPs (at the same Pd charge as that for 30 sc% In-on-Pd NPs) were also conducted. To verify that  
46 intimate contact between the In and Pd was required, we carried out a control experiment using a  
47 combination of 10 mg of In<sub>2</sub>O<sub>3</sub> and 3.51 mg (1.15 mL of 3.05 mg Pd/mL solution) Pd NPs.  
48  
49  
50  
51  
52  
53  
54  
55  
56  
57  
58  
59  
60

1  
2  
3 Unlike the NP-only experiments, the supported Pd catalysts and In<sub>2</sub>O<sub>3</sub> powder had significant  
4 absorbance in the visible light regime, and the powder was separated from the reaction medium  
5 with syringe filters (0.45- $\mu$ m PES filter media) before nitrate, nitrite and ammonium  
6 concentrations were determined.  
7  
8  
9  
10

11  
12 Nitrite concentrations were analyzed using the Griess test.<sup>45</sup> A stock solution of the Griess  
13 reagent was prepared by dissolving 0.1 g of N-(1-naphthyl)ethyl-enediamine dihydrochloride, 1.0  
14 g of sulfanilamide and 2.94 mL H<sub>3</sub>PO<sub>4</sub> in 100 mL DI water, such that the final concentrations  
15 were 0.1 wt% N-(1-naphthyl)ethyl-enediamine dihydrochloride, 1 wt% sulfanilamide, and 5%  
16 H<sub>3</sub>PO<sub>4</sub>.<sup>46</sup> In a typical colorimetric assay (concentration range from 0.02 to 2.5 ppm), the Griess  
17 reagent solution (0.2 mL), a nitrite-containing solution (0.2 mL), and water (1.6 mL) were mixed  
18 together and allowed to react at room temperature for 10 min, after which no further color  
19 change was observed. The sulfanilamide reacts with the nitrite anion to form a diazonium salt,  
20 which further reacts with the amine to form an azo dye (magenta in color). The absorbance at  
21 540 nm is measured via UV-vis spectroscopy, and the NO<sub>2</sub><sup>-</sup> concentration is determined in the 0  
22 to 2.0 ppm range using a standard calibration curve. Nitrate and ammonium measurements were  
23 made using a nitrate ion selective electrode (Cole-Parmer, lower detection limit 0.1 ppm) and an  
24 ammonium ion selective electrode (Cole-Parmer, lower detection limit 0.01 ppm).  
25  
26  
27  
28  
29  
30  
31  
32  
33  
34  
35  
36  
37  
38  
39  
40  
41

42 The observed reaction rate constant  $k_{\text{meas}}$  (with unit of min<sup>-1</sup>) was calculated by assuming  
43 pseudo first-order dependence on nitrate concentration (H<sub>2</sub> gas was in excess):  
44

$$45 \quad -\frac{dC_{\text{NO}_3^-}}{dt} = k_{\text{meas}} C_{\text{NO}_3^-}$$

46  
47  
48  
49  
50  
51 where  $C_{\text{NO}_3^-}$  is the concentration of nitrate (with units of mg L<sup>-1</sup>) and  $t$  is reaction time (with  
52 units of min).  
53  
54  
55  
56  
57  
58  
59  
60

Using methods described in our previous work<sup>20,44</sup> and in the Supporting Information, mass transfer effects were quantified by varying the mass loading of catalyst at a constant stir rate. We used 40 sc% In-on-Pd NPs as the test case, such that the metal content varied (1.75 mg, 3.51 mg, and 5.26 mg Pd NPs, and 277, 553, and 830  $\mu\text{g}$  In, respectively) while keeping the total reaction volume constant at 99.5 mL.

The measured rate constants were corrected for gas-liquid mass transfer to obtain the corrected rate constant  $k_{corr}$  values. The surface metal normalized reaction rate constant  $k_{cat}$  (with units of  $\text{L g}_{\text{surface metal}}^{-1} \text{min}^{-1}$ ) was then calculated from  $k_{corr}$  (via  $k_{cat} = k_{corr}/C_{cat}$ , where  $C_{cat}$  is the total concentration of amount of surface In and Pd in the reaction medium; with units of  $\text{g}_{\text{surface metal}} \text{L}^{-1}$ ).

The initial molar concentration of nitrate and the concentration of nitrate after time  $t$  are  $C_0$  and  $C$ . Prior studies indicate that only trace amounts of intermediate products NO and  $\text{N}_2\text{O}$  are formed in the bulk during nitrate reduction.<sup>28,29,42</sup> Thus we calculate the selectivity to  $\text{N}_2$  ( $S_{\text{N}_2}$ ) in the following way:

$$S_{\text{N}_2} = 100\% - S_{\text{NH}_4^+} - S_{\text{NO}_2^-}$$

where the selectivity to ammonium and selectivity to nitrite ( $S_{\text{NH}_4}$  and  $S_{\text{NO}_2}$  respectively) are

$$S_{\text{NH}_4^+} = \left( \frac{C_{\text{NH}_4^+}}{C_0 - C} \right) \times 100\%$$

and

$$S_{\text{NO}_2^-} = \left( \frac{C_{\text{NO}_2^-}}{C_0 - C} \right) \times 100\%$$

respectively.

## Computational methodology

All periodic density functional theory (DFT)<sup>47</sup> calculations were performed using the Vienna *ab-initio* simulation (VASP) package.<sup>48-51</sup> Electron exchange and correlation were described by the revised Perdew-Burke-Ernzerhof (GGA-RPBE) functional.<sup>52,53</sup> The projector augmented wave (PAW)<sup>54,55</sup> method was used to describe the core and valence electrons with a kinetic energy cut-off of 400 eV for surfaces and 540 eV for bulk materials. Partial occupancies for the wavefunctions were calculated using Gaussian smearing<sup>56</sup> with a Fermi temperature ( $k_bT$ ) of 0.1 eV. The total energies were extrapolated to  $k_bT = 0$  eV at the end of ionic convergence. Bader charge analysis<sup>57-60</sup> was performed to assess the extent of oxidation of the indium atoms.

A flat Pd(111) surface was constructed using a (4×4) unit cell, and a (1×3) unit cell was used to describe the stepped Pd(211) surface. For both structures we used an equivalent of four atomic layers, where the top two layers were fully relaxed and the bottom two layers were fixed at their bulk positions corresponding to the optimized lattice constant value of 3.99 Å. A vacuum of 20 Å was added along the z axis normal to the surface along with the corresponding dipole correction.<sup>61</sup> For the bulk and surface calculations a (13×13×13) and (4×4×1) Monkhorst-pack k-point mesh<sup>62</sup> were used, respectively. The bulk structure of Indium was also optimized using the RPBE functional, with the initial crystal structure obtained from ICSD.<sup>63,64</sup> The final optimized lattice constants were  $a = 3.34$  Å,  $b = 3.35$  Å,  $c = 5.10$  Å. The monometallic In(001) surface was constructed using a (2×2) unit cell, with a (4×4×1) Monkhorst-pack k-point mesh and other calculation settings were kept consistent with the palladium system.

The bimetallic In-on-Pd models were created by successively replacing Pd(111) surface atoms with In, as shown in Figure 1. The In sc% was then approximated by the number of indium atoms in the surface divided by the total number of surface atoms, *e.g.*, a substitution of 4 Pd atoms with In in a (4×4) unit cell yields  $4/16 = 25$  sc% In. When the In surface coverage reached 50 sc%, the larger In atoms could no longer be accommodated in the Pd lattice without causing significant surface buckling and reconstruction. Thus, we increased the Pd(111) unit cell to (6×6) and added a layer of 25 In atoms to reduce the surface strain when modeling a full monolayer of In on Pd(111) (100 sc%). Here a (3×3×1) Monkhorst-pack k-point mesh was used.

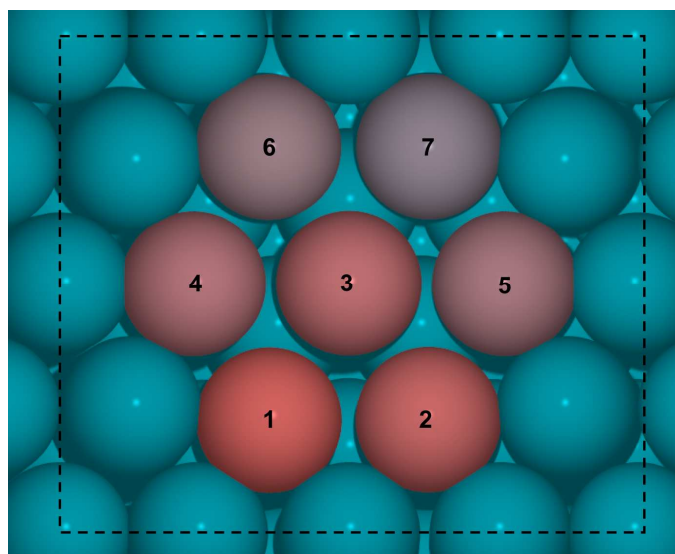
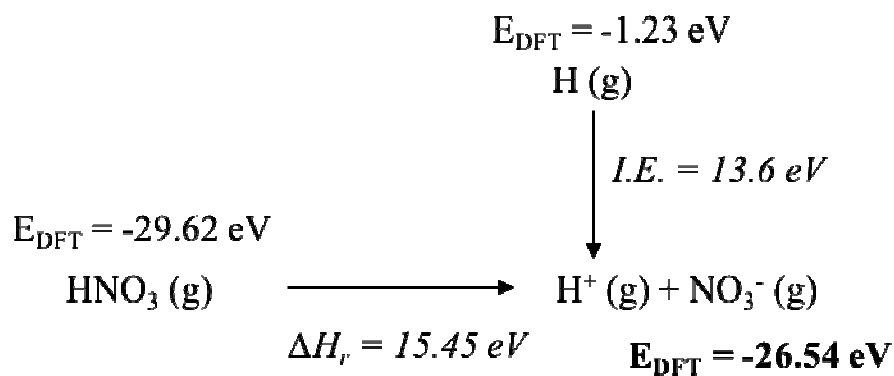


**Figure 1.** Successive In atom (red) substitution in a Pd(111) 4×4 unit cell to form compact In ensembles. The progressive substitution sequence is indicated by the numerals 1-7 and a decreasing red color intensity. Substitution of all seven sites results in a nominal In surface content of  $7/16 = 43.8$  sc%.

To avoid problems of using periodic DFT methods to describe the charged  $\text{NO}_3^-$  species as reference, we used neutral  $\text{HNO}_3$  as gas phase reference instead, and obtained the energy for the nitrate ion according to the thermodynamic cycle shown in Scheme 1. This reference neglects the solvation energy,  $\Delta G_{sol}$ , of nitrate ions in aqueous environment. Since the value of  $\Delta G_{sol}$  is

constant when different catalysts are compared, we chose to lump it as a first order approximation into the estimation of the equilibrium constant for nitrate adsorption. Upon adsorption on the metal surface we further assume that any charges on adsorbates are quenched and delocalized throughout the metal, such that surface energetics are expected to be within typical DFT errors. Despite our best efforts to make reasonable assumptions for the adsorption and reaction of the charged nitrate species in aqueous solution, this approach is subject to uncertainties as a result of neglecting the explicit treatment of the negative charge and solvation effects. The solvent does not only stabilize the nitrate ion in solution, but also alters the energetics of adsorbed (possibly charged) species and empty surface sites. Reliable quantification methods for these effects are currently unavailable, but we estimate that the catalyst-adsorbate interactions across our model systems outweigh the significance of solvation effects for similar surface intermediates and transition states. The gas phase energy values for H, H<sub>2</sub>, H<sub>2</sub>O, HNO<sub>3</sub>, and N<sub>2</sub> were obtained from Gamma point only calculations by placing a single molecule in a cubic box with edges of 10 Å.



**Scheme 1.** Thermodynamic cycle to estimate the reference DFT energy for the NO<sub>3</sub><sup>-</sup> ion using reference values for the ionization energy of H (*I.E.*)<sup>65</sup> and the heat of reaction for HNO<sub>3</sub>(g) deprotonation ( $\Delta H_r$ ).<sup>66</sup>

1  
2  
3 Transition state geometries were found using the climbing image nudged elastic band  
4 (NEB)<sup>67–72</sup> and dimer methods.<sup>73–76</sup> A single imaginary mode in the subsequent vibrational  
5 analysis using the harmonic oscillator approximation and a Cartesian displacement of 0.01 Å  
6 verifies these geometries as true saddle points.  
7  
8  
9  
10

11  
12 All rate constants in the lumped kinetic model are estimated from free energies obtained  
13 from first principles and corrected for the zero-point energy, enthalpy and entropy contributions  
14 at 300 K. For adsorbed species, we obtained these corrections from a frequency analysis in the  
15 harmonic oscillator approximation. For gas phase free energies, we adopted enthalpy and entropy  
16 corrections calculated using the Shomate equation and gas phase partial pressures totaling 1 bar.  
17  
18  
19  
20  
21  
22  
23  
24  
25

## 26 **Results and discussion**

27  
28 Representative TEM images for Pd NPs and 110% sc In-on-Pd NPs are shown in Figure 2. The  
29 bare Pd NPs were monodisperse, with a mean diameter of 5.0±0.4 nm. The addition of In slightly  
30 increased the particle size. The sample with the most In, 110% sc In-on-Pd NPs (*e.g.*, more than  
31 one calculated monolayer of In on the Pd NPs) had a mean diameter of 5.7±0.6 nm.  
32  
33  
34  
35  
36  
37  
38  
39  
40  
41  
42  
43  
44  
45  
46  
47  
48  
49  
50  
51  
52  
53  
54  
55  
56  
57  
58  
59  
60

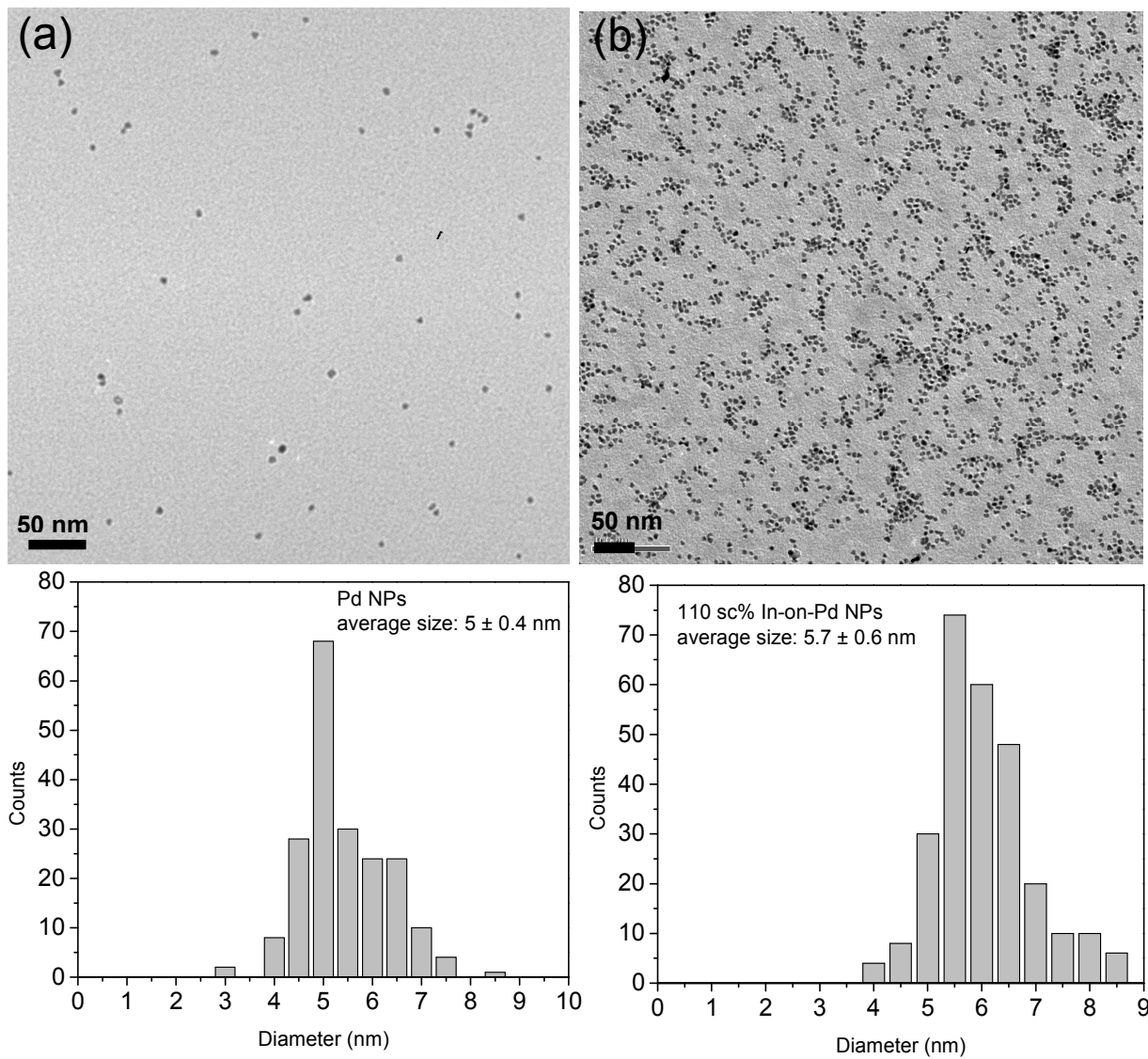
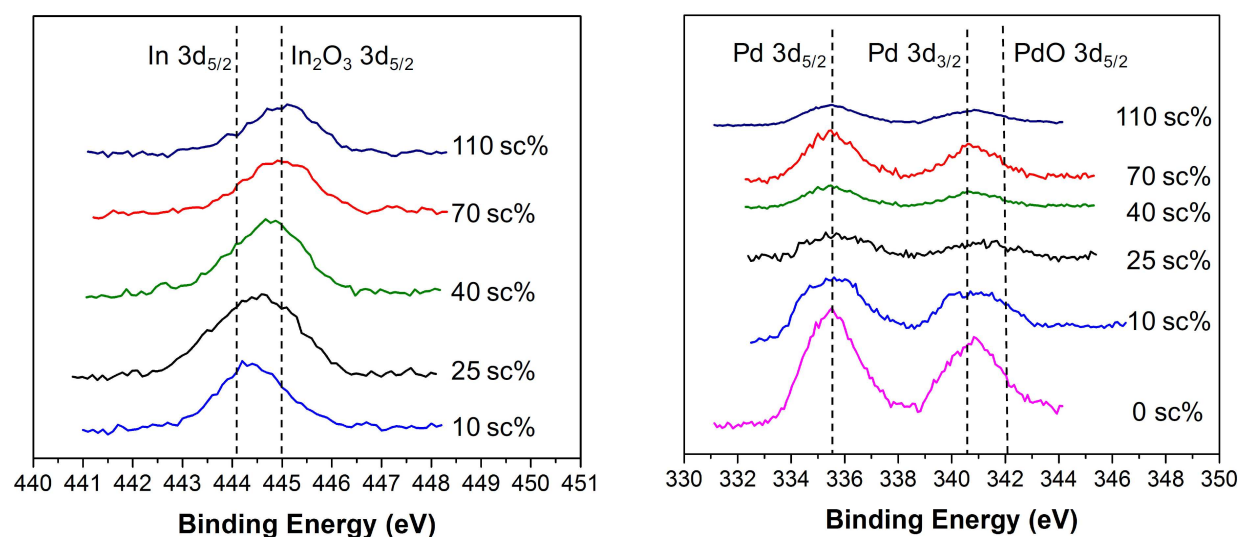


**Figure 2.** Transmission electron microscopy (TEM) images and corresponding particle size distributions of (a) Pd NPs and (b) In-on-Pd NPs (with 110 sc% In). Each bar represents the total count percentage of NPs with a measured diameter  $\pm 0.25$  nm.

The XPS spectra of the Pd NPs and In-on-Pd NPs with 10-110 sc% are shown in Figure 3. Figure 3a shows the spectra between 440-450 eV, the region for the In  $3d_{5/2}$  peak (previous literature reports the  $\text{In}_2\text{O}_3$  peak at 445 eV and the peak for In(0) is reported to be around 444 eV).<sup>77</sup> As can be seen, the peak binding energy blueshifted with added In, from 444.2 eV (for the 10 sc% In-on-Pd NPs) to 444.9 eV (for the 110 sc% Pd-on-In NPs), indicating that the Pd had an

1  
2  
3 electronic effect on the In; the samples with lower loadings had more of a reduced character. On  
4  
5 the other hand, the electronic state of Pd was unaffected by the In (Figure 3b). The peak at 335.5  
6  
7 eV matches that reported for Pd 3d<sub>5/2</sub> for Pd(0), and the peak at 340.5 eV can be attributed to the  
8  
9 Pd 3d<sub>3/2</sub> for Pd(0). The shoulder for the latter peak could be due to the presence of oxidized Pd  
10  
11 (the Pd<sub>3/2</sub> of PdO is 342 eV) which possibly formed during sample preparation and storage at  
12  
13 atmospheric conditions. Unlike the In peak, the Pd peaks did not shift with In loading.  
14  
15  
16  
17  
18  
19



20  
21  
22  
23  
24  
25  
26  
27  
28  
29  
30  
31  
32  
33  
34  
35  
36  
37 **Figure 3.** XPS spectra of In-on-Pd NPs with different surface coverages: (a) In 3d<sub>5/2</sub> energy  
38 range and (b) Pd 3d energy range.  
39  
40

41  
42 To further verify the oxidation state of In and Pd in the In-on-Pd NPs and also infer more  
43 information about the catalysts, we used X-ray absorption spectroscopy (XAS). We have  
44 previously used this technique to extensively characterize the surface structure of Pd-on-Au NP  
45 catalysts for various reactions.<sup>20,36,39</sup> Figure 4a shows the XAS results of the Pd edge for Pd NPs  
46 and In-on-Pd NPs of different surface coverages and with different pretreatments (as-synthesized  
47 and reduced in H<sub>2</sub>, Table S6).  
48  
49  
50  
51  
52  
53  
54  
55  
56  
57  
58  
59  
60

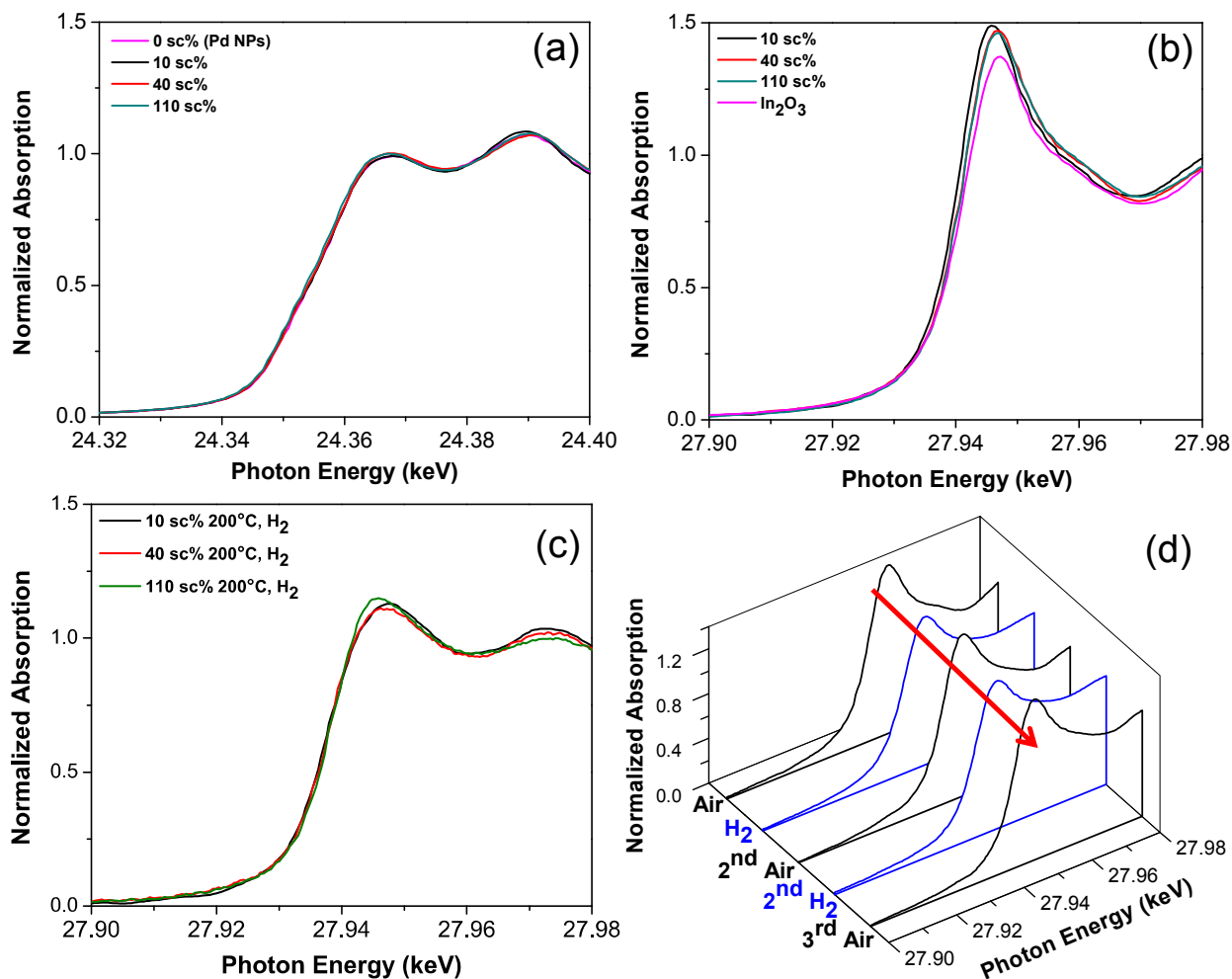


**Figure 4.** XANES spectra of the as-synthesized samples at the (a) Pd K and (b) In K edges. (c) XANES spectra (at In K edge) of In-on-Pd NPs with different In sc% after reduction with H<sub>2</sub> at 200 °C. (d) *in situ* XANES (In K edge) of the 40 sc% In-on-Pd NPs under cycles of air- and 4% H<sub>2</sub>-saturated water at room temperature.

In agreement with the XPS data, the spectra showed that regardless of pretreatment and composition, all samples had zero-valent Pd. We note that this is in contrast to our previous results,<sup>37,39,40</sup> which showed that monometallic Pd NPs were partially oxidized after handling in air. We attribute this to the presence of PVP, as other researchers have also observed the absence of oxidized metal in metal NPs prepared using PVP.<sup>78,79</sup> Significantly, the Pd-Pd bond distance was close to 2.75 Å (Table S6) for all the catalysts, and is identical to bulk Pd, suggesting that the In did not alloy into the Pd NPs and remained on the NP surface. In contrast, fully alloyed

1  
2  
3 PdIn nanoparticles have EXAFS observable Pd-In bond distances of 2.81 Å,<sup>80</sup> which were not  
4  
5 observed here.  
6

7  
8 The amount of oxidized In in the samples can be estimated by dividing the In-O  
9  
10 coordination number determined from EXAFS analysis of the In edge by six, since In  
11  
12 coordinated with six O atoms is consistent with fully oxidized In<sup>3+</sup>. As prepared, the In was fully  
13  
14 oxidized ("In(OH)<sub>3</sub>") for all the catalysts, and no In-In scattering pairs were detected (Table S6).  
15  
16 Exposure of the catalysts to 4% H<sub>2</sub> gas at 200 °C for 30 min was sufficient to partially reduce the  
17  
18 In, leading to In-In scattering pairs with nonzero coordination numbers. In-on-Pd NPs with the  
19  
20 10 sc%, 40 sc%, and 110 sc% contained 65%, 60%, and 45% In as zerovalent metal, respectively,  
21  
22 after reduction treatment (Figure 4c, Table S2). This result suggested the presence of oxidized In  
23  
24 that can be reduced under reaction conditions.  
25  
26

27  
28 We gained additional insights about the state of In metal in the In-on-Pd NPs, after  
29  
30 analysis of the calculated free energies of In atoms in different positions on Pd terraces and steps  
31  
32 (Figure 5). An In adatom on the Pd(111) surface is highly mobile and can diffuse with an  
33  
34 activation barrier of less than ~0.1 eV to a Pd (211) step, where it is ~0.7 eV more stable (Fig.  
35  
36 5a-b). Its stability further increases by ~0.2 eV if it replaces a higher coordinated Pd atom in the  
37  
38 (111) surface (Fig. 5c). If located in a fully coordinated subsurface layer position though, In is  
39  
40 0.05 eV less stable (Fig. 5d). 2D In ensembles containing 7 atoms or less are energetically more  
41  
42 stable compared to a single In adatom, with an energy penalty that increases with ensemble size  
43  
44 (Figures 5e-j). The 2D ensembles may grow to form a monolayer of In atoms as illustrated in  
45  
46 Figures 5k, or further agglomerate to form 3D In clusters as depicted in Figure 5l. We did not  
47  
48 attempt to model Pd-supported In clusters; instead we chose to approximate them as pure In(001).  
49  
50  
51  
52  
53  
54  
55  
56  
57  
58  
59  
60

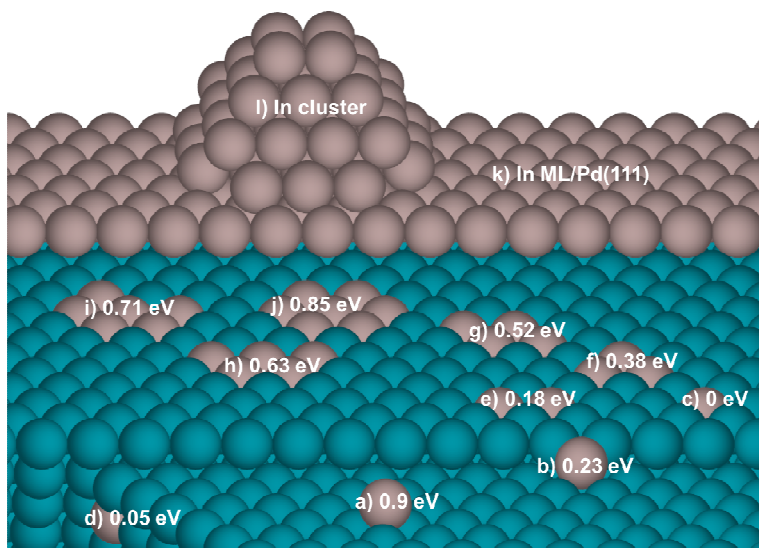


**Figure 5.** Stability of In atoms on Pd relative to the most stable configuration: (a) In adatom on Pd(111) terrace; (b) In adatom at Pd(211) step; (c) In atom substitution in the top layer; (d) In atom substitution in 1<sup>st</sup> sublayer of Pd(111); 2D In ensembles within the Pd(111) top layer containing (e) 2, (f) 3, (g) 4, (h) 5; (i) 6, and (j) 7 In atoms; (k) In monolayer (ML) on Pd(111) (equivalent to 100 sc%); and (l) a schematic 3D In ensemble.

The combined experimental and computational characterization of the In-on-Pd NPs are largely consistent with metallic In substituting Pd on surface terrace sites. At low In sc%, In atoms are well-dispersed and remain metallic. The theoretical maximum In surface concentration on Pd(111) with isolated In atoms is 33 sc%, suggesting that the In-on-Pd NPs contain 2D and 3D ensembles at higher In content. The In-rich materials are expected to show more bulk In metal character and are more likely to oxidize.

### Nitrate reduction catalytic behavior

Figure 6 shows a representative plot of the time evolution of nitrate, nitrite, ammonium and dinitrogen concentrations on the 40 sc% In-on-Pd catalyst sample. The decrease in nitrate concentration fit well to a pseudo first-order model, and the observed reaction rate constant,  $k_{meas}$ ,

was obtained from the slope of the natural log of nitrate concentration versus reaction time using linear least squares fitting.

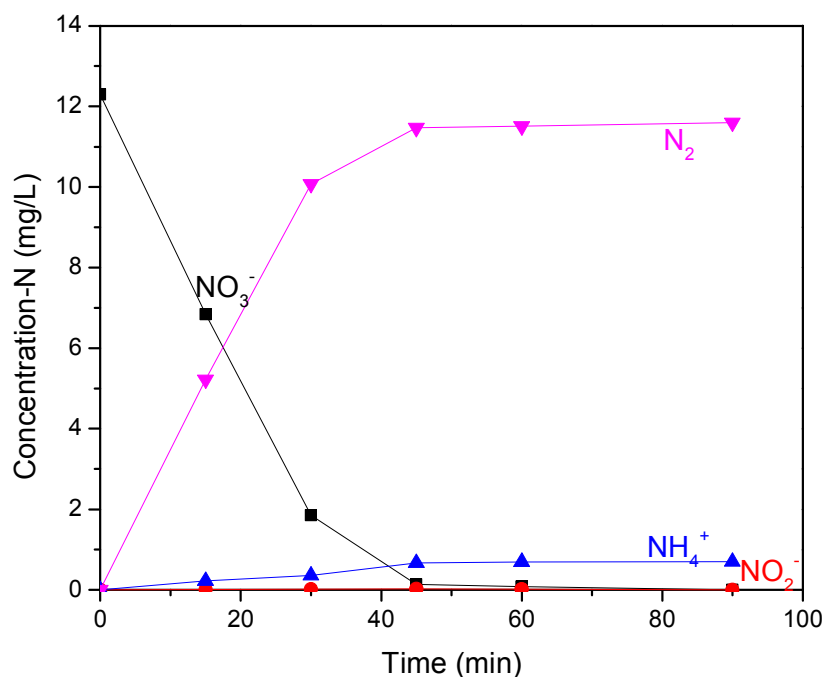


**Figure 6.** Concentration-time curves of  $\text{NO}_3^-$ ,  $\text{NO}_2^-$ ,  $\text{NH}_4^+$  and  $\text{N}_2$ . Reaction conditions: 40 sc% In-on-Pd NPs with 0.553 mg/L In in reactor, 600 rpm stirring rate, 1 atm pressure, 120 mL/min  $\text{H}_2$ , 120 mL/min  $\text{CO}_2$ , pH = 5. The initial nitrate/indium molar ratio was 166/1.

Control experiments using  $\text{In}_2\text{O}_3$ , Pd NPs, and 1 wt% Pd/ $\text{Al}_2\text{O}_3$  all showed that the monometallic catalysts are inactive for nitrate reduction (Table 1). Thus catalytic activity was quantified by normalizing the mass transfer corrected  $k_{meas}$  to total surface metal content ( $k_{cat}$ ), not to surface Pd or surface In content.

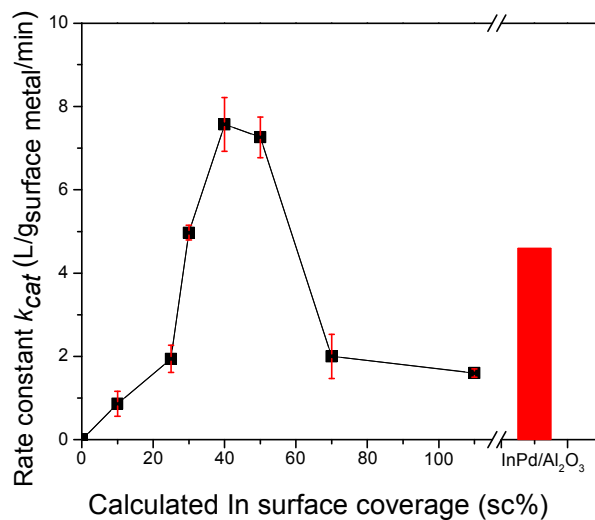
**Table 1.** Rate constants for In-on-Pd NPs, Pd/ $\text{Al}_2\text{O}_3$ , In-Pd/ $\text{Al}_2\text{O}_3$  and  $\text{In}_2\text{O}_3$

Sample name	$k_{meas}$ ( $\text{min}^{-1}$ )	$k_{corr}$ ( $\text{min}^{-1}$ )	$k_{cat}$ ( $\text{L g}_{\text{surface metal}}^{-1} \text{min}^{-1}$ ) <sup>a</sup>
0 sc% In-on-Pd NPs	inactive	inactive	inactive
10 sc% In-on-Pd NPs	0.032±0.01	0.035	0.86±0.30
25 sc% In-on-Pd NPs	0.031±0.0056	0.034	1.94±0.32
30 sc% In-on-Pd NPs	0.059±0.002	0.072	4.97±0.18
40 sc% In-on-Pd NPs	0.069±0.015	0.087	7.57±0.65

50 sc% In-on-Pd NPs	0.057±0.013	0.069	7.26±0.49
70 sc% In-on-Pd NPs	0.014±0.003	0.015	2±0.53
110 sc% In-on-Pd NPs	0.0086±0.0005	0.0088	1.6±0.10
In <sub>2</sub> O <sub>3</sub> powder	inactive	inactive	inactive
Pd NPs	inactive	inactive	inactive
Pd/Al <sub>2</sub> O <sub>3</sub> (1 wt% Pd)	inactive	inactive	inactive
Pd NPs and In <sub>2</sub> O <sub>3</sub> physical mixture	inactive	inactive	inactive
In/Pd/Al <sub>2</sub> O <sub>3</sub> (0.13 wt% In, 1 wt% Pd)	0.075	–	4.6

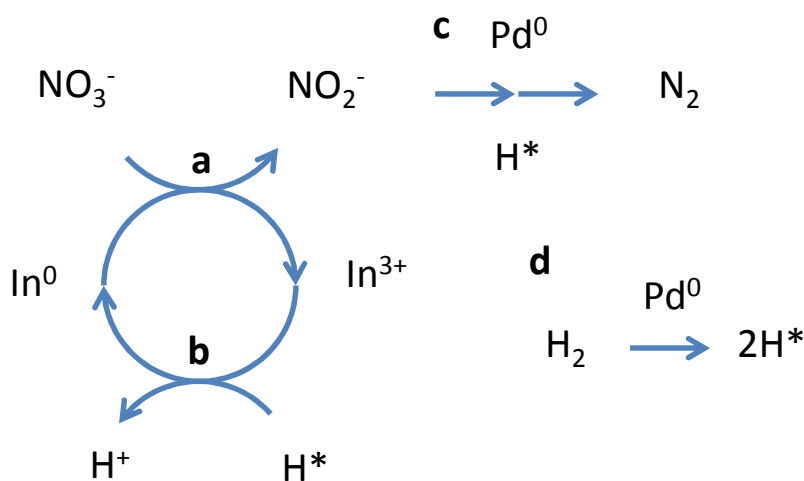
<sup>a</sup>Calculated from  $k_{corr}$  and magic cluster model

Figure 7 shows that the activity of In-on-Pd NPs (as assessed by  $k_{cat}$ ) demonstrating the volcano-shape dependence on In surface coverage. The rate constants increased from 0 sc% to 40 sc% and decreased from 40 sc% to 110 sc%. Maximum nitrate reduction was measured at 40 sc% with  $k_{cat} = 7.57 \text{ L}^{-1} \text{ g}_{\text{surface metal}}^{-1} \text{ min}^{-1}$ . The In/Pd/Al<sub>2</sub>O<sub>3</sub> supported catalyst contained the same Pd and In mass ratio as the 40 sc% NP material but showed 60% less activity, attributable to the deposition of inactive indium on the Al<sub>2</sub>O<sub>3</sub> support surface.



**Figure 7.** Experimentally determined nitrate reduction rate constants for In-on-Pd NPs as a function of In surface coverage and for In/Pd/Al<sub>2</sub>O<sub>3</sub> (1 wt% Pd, 0.13 wt% In).

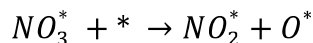
The catalytic nitrate reduction reaction presumably involves a bifunctional effect in which the In-on-Pd NPs carry two active site types that participate in different parts of the surface reaction pathway. The In site has the primary role of adsorbing and reducing nitrate from solution, and the Pd site has the roles of generating hydrogen adatoms; reducing the surface nitrite species; and reducing the oxidized In via hydrogen spillover (Scheme 2). The activity of the In-on-Pd NPs increased with indium amounts at surface coverages below 40 sc%, where isolated In atoms and small In ensembles prevail. These sites adsorb and convert more nitrate, which leads to a higher reaction rate. However, deposition of too much In is counterproductive, as large In ensembles may block Pd active sites necessary for dissociating hydrogen used in the further reduction of nitrite and regeneration of metallic In sites.



**Scheme 2.** Schematic illustration of the nitrate reduction mechanism using In-on-Pd NPs.  $\text{H}^*$  represents hydrogen atoms adsorbed on the Pd surface. (a) Reduction of nitrate to nitrite and oxidation of  $\text{In}^0$  to  $\text{In}^{3+}$ , (b) regeneration of  $\text{In}^0$  by  $\text{H}^*$ , (c) further reduction of nitrite to dinitrogen over  $\text{Pd}^0$ , and (d) dissociation of  $\text{H}_2$  into  $\text{H}^*$  over  $\text{Pd}^0$ .

Further support for the synergistic effect of the bimetallic In-on-Pd NPs for nitrate reduction was provided by DFT simulations on a Pd(111) surface with ensembles of varying

1  
2  
3 number of In atoms and monometallic Pd and In surfaces. Since the Pd ability to reduce nitrite is  
4 well established<sup>15,17,19,20,81–83</sup>, we focused only on the following elementary reactions (nitrate  
5 adsorption and oxygen abstraction) and assume all other steps to be fast (\* represents the active  
6 site):  
7  
8  
9  
10  
11



12  
13  
14  
15  
16  
17 Figure 8 shows the transition state geometries of the two reaction steps on selected  
18 geometries and their corresponding free energy diagrams. A complete description of all initial  
19 states (IS), transition states (TS), final states (FS), and the reaction energetics is provided in  
20 Figure S3. While an isolated In atom (Figure 8b) did not promote nitrate binding or activation  
21 compared to monometallic Pd(111) (Figure 8a), a small 3-In-atom ensemble (18.8 sc%) did  
22 result in stronger nitrate binding and higher oxygen abstraction activity. Notably, the In trimer  
23 stabilized either the IS (Figure 8c) or FS (Figure 8d). The In promotion effect was more  
24 pronounced (*i.e.*, a lower activation barrier) when the dissociated O atom was located in the 3-  
25 fold hollow site in the FS (Figure 8d).  
26  
27  
28  
29  
30  
31  
32  
33  
34  
35  
36

37  
38 Adding a fourth In atom into this ensemble (25 sc%) resulted in a substantial  
39 improvement, because the IS, TS, and FS were all stabilized simultaneously by In atoms  
40 throughout the reaction path. Increasing the ensemble size to 6 In atoms (37.5 sc%, Figure 8f)  
41 lowered the activation barrier further, but this was associated with a weaker binding of the final  
42 state. The weaker binding of the final state was consistent with increased compressive lateral  
43 strain caused by the larger In atoms. In fact, substituting a 7<sup>th</sup> In atom into the Pd(111) (4×4) unit  
44 cell resulted in sufficient lattice strain to cause surface buckling (43.8 sc%, Figure 8g).  
45  
46  
47  
48  
49  
50  
51  
52  
53  
54  
55  
56  
57  
58  
59  
60

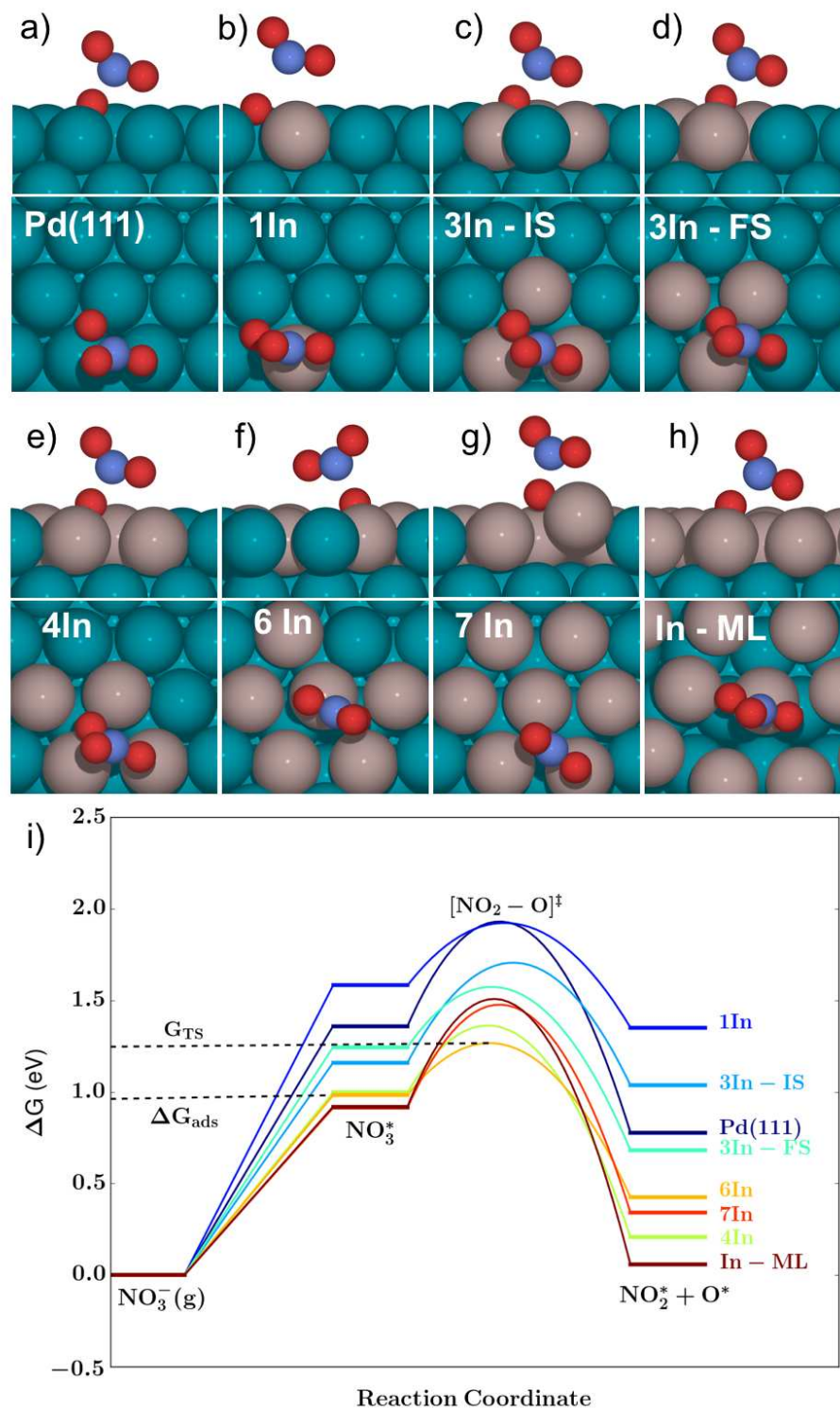


**Figure 8.** Nitrate reduction pathways. (a)-(h) side and top view of the TS geometry on selected Pd(111)/In ensembles. (a) 0 sc% (b) 6.3 sc%, one In atom, (c) 18.8 sc% ,In trimer (IS favored), (d) 18.8 sc%, In timer (FS favored), (e) 25.0 sc% , In 4-mer, (f) 37.5 sc%, In 6-mer, (g) 43.8 sc%, In 7-mer), and (h) 100 sc%, In monolayer. (i) Free energy diagram for nitrate adsorption and

1  
2  
3 oxygen abstraction on the same selected Pd(111)/In ensembles. The nitrate adsorption energy  
4 ( $\Delta G_{ads}$ ) and the transition state free energy ( $G_{TS}$ ) for the In 6-mer are marked as example.  
5  
6

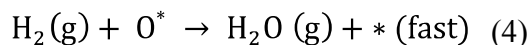
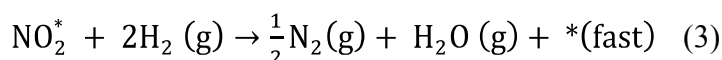
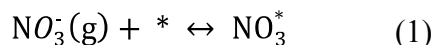
7 In an attempt to lower the compressive strain in the limiting case of 1 ML In on Pd(111),  
8 we used an enlarged (6×6) Pd(111) unit cell and added a ML with only 25 In atoms. The average  
9 In-In distance in the relaxed ML structure became 3.1 Å, but there was still some compressive  
10 strain compared to the In-In bulk distance of 3.35 Å. While this In monolayer model had the  
11 strongest stabilization of the dissociated final state, the calculated dissociation barrier was greater  
12 than in the 4- or 6-atom ensembles. These results demonstrate that the ensemble size and its  
13 atomic arrangement greatly influence the synergistic effect of In-on-Pd NPs and that an optimal  
14 In sc% can be expected.  
15  
16  
17  
18  
19  
20  
21  
22  
23  
24

25 We can generally conclude from the free energy diagram (Figure 8i) corroborates the  
26 notion that In promotes nitrate adsorption, and that In ensembles of 4-6 atoms have the lowest  
27 activation barrier for N-O bond cleavage. Yet, the IS, TS, and FS of nitrate reduction do not  
28 follow a consistent trend with increasing ensemble size and multiple overlaps in the free energy  
29 diagram exist. A direct interpretation of this free energy diagram in terms of nitrate reduction  
30 activity is not straightforward because a lower N-O scission barrier may be compensated by  
31 weaker NO<sub>3</sub>\* binding, *i.e.*, lower NO<sub>3</sub>\* coverage, and vice versa. This motivated us to develop a  
32 qualitative kinetic model to predict ensemble effects on the nitrate reduction rate.  
33  
34  
35  
36  
37  
38  
39  
40  
41  
42  
43  
44  
45

#### 46 Kinetic modeling

47 We used a simple lumped kinetic model to understand the promotional effect of In on Pd for  
48 nitrate reduction leading to the remarkable activity of In-on-Pd catalysts. The kinetic model was  
49 developed to qualitatively explain activity changes with In content, and quantitative agreement  
50 was not expected. In this model, the adsorption of a nitrate ion is quasi-equilibrated, followed by  
51  
52  
53  
54  
55  
56  
57  
58  
59  
60

an irreversible  $\text{NO}_3^*$  reduction to  $\text{NO}_2^*$  and  $\text{O}^*$ . Since Pd is known to rapidly reduce  $\text{NO}_2^*$  to  $\text{N}_2$  or  $\text{NH}_3$ , we assumed that the remaining elementary reaction steps are fast and not rate-limiting. Thus, this model helps us understand how each of these catalyst models perform for the initial  $\text{NO}_3^*$  to  $\text{NO}_2^*$  reduction step. The simplified reaction mechanism is written as:



We note that this lumped mechanism fails for active sites that easily oxidized, such that oxygen removal becomes rate-limiting (step 4). Similarly, the catalyst must be a good  $\text{NO}_2^-$  reduction catalyst for step 3 to be fast. Under the stated assumptions, we derived an analytical expression for the  $\text{NO}_3^-$  reduction rate. Using the quasi-equilibrium approximation for step 1 we obtain

$$\theta_{\text{NO}_3} = K_1 C_{\text{NO}_3} \theta_*$$

The forward rate of the irreversible step 2 is then

$$r_2 = k_2^+ \theta_{\text{NO}_3} \theta_* = K_1 k_2^+ C_{\text{NO}_3} \theta_*^2$$

in which  $K_1$  is the equilibrium constant for reversible  $\text{NO}_3^-$  adsorption calculated from  $\Delta G_1 = \Delta G_{\text{ads}} - \Delta G_{\text{sol}}$ ,  $k_2^+$  is the forward reaction rate constant for  $\text{NO}_3^*$  reduction,  $C_{\text{NO}_3}$  is the nitrate concentration, and  $\theta_{\text{NO}_3}$  and  $\theta_*$  are the surface coverages of  $\text{NO}_3^*$  and vacant sites ‘\*’, respectively.

Finally, we assumed that all active site models have a similar fraction of empty sites, because the adsorption of  $\text{NO}_3^-$  is highly endothermic as shown in Figure 8, hydrogen binds weakly as we discuss later in Figure 10, and  $\text{NO}_2^*$  disappears quickly on Pd sites. This leaves  $\text{O}^*$  as the most important surface intermediate to consider, but as previously stated, the simplified

1  
2  
3 model assumes that O\* removal is not rate-limiting. If the fraction of vacant sites is similar, then  
4  
5 the  $\theta_*^2$  term cancels out when we define the final expression for the NO<sub>3</sub> reduction rate  $r'$  relative  
6  
7 to Pd(111)  
8

$$r' = \frac{K_1 k_2^\ddagger}{K_{1,Pd(111)} k_{2,Pd(111)}^\ddagger}$$

9  
10  
11  
12  
13 At this point we note that the constant contribution of  $\Delta G_{sol}$  to  $K_1$  on different catalyst models  
14  
15 also cancels out and we consider only  $\Delta G_{ads}$  for the estimation of  $K_1$ . This relative rate of  
16  
17 disappearance of nitrate species is shown for all investigated In ensemble models in Figure 9a.  
18  
19 The 6-atom In ensemble, corresponding to 37.5 sc%, outperforms all other tested ensembles and  
20  
21 coincides with the experimentally determined activity peak between 40-50 sc% (Figure 7). From  
22  
23 the semi-log scale plot in Figure 9b one can more clearly see that In ensembles of 4 or more  
24  
25 atoms (>25 sc%) show a drastically improved nitrate reduction rate (6 orders of magnitude or  
26  
27 more) that extends to 100 sc%. It can also be shown that the effective, lumped rate constant  
28  
29  $K_1 k_2^\ddagger$  implies that the apparent activation energy is equal to the transition state energy  $G_{TS} =$   
30  
31  $\Delta G_{ads} + E_a$ , where  $\Delta G_{ads}$  describes the free energy of nitrate adsorption and  $E_a$  is the activation  
32  
33 barrier for nitrate reduction. Thus, the high activity for the 6-atom In ensemble can be attributed  
34  
35 to its low transition state energy  $G_{TS}$  in Figure 8i.  
36  
37  
38  
39  
40  
41  
42  
43  
44  
45  
46  
47  
48  
49  
50  
51  
52  
53  
54  
55  
56  
57  
58  
59  
60

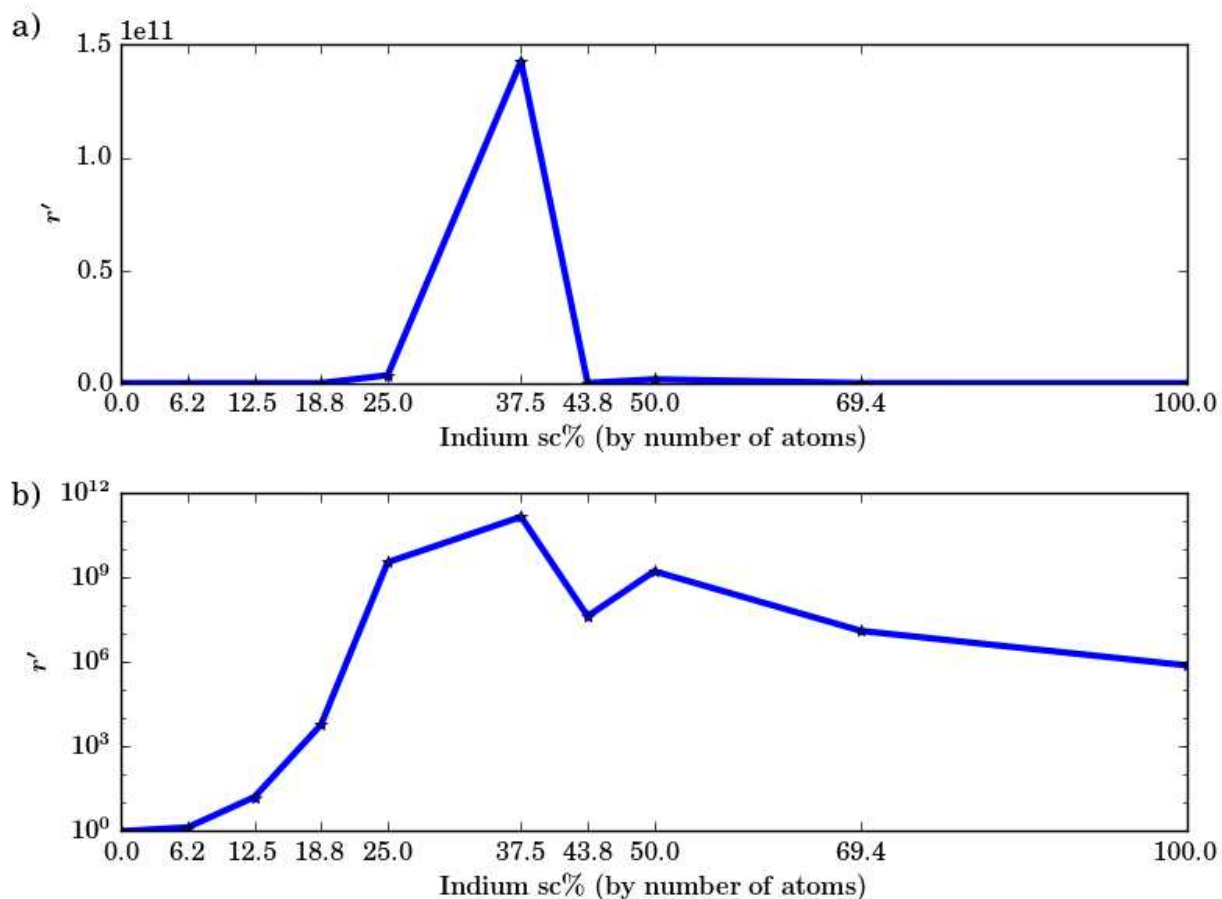


**Figure 9.** Nitrate reduction rate  $r'$  relative to pure Pd(111) as function of In sc% in (a) linear scale and (b) semi-log scale.

Overall, the theoretical results support the first part of our hypothesis, namely that In atoms are necessary to improve nitrate adsorption and lower the transition state energy for nitrate reduction. As discussed in the previous section, the key contribution of In to stabilize the nitrate abstraction transition state stems from its affinity towards oxygen. This may ultimately prove detrimental, however, when the In ensembles become so large that they resemble bulk In and form an oxide phase, rendering our assumption of rapid oxygen removal invalid.

### Removing oxygen from In ensembles

Oxygen removal as water according to reaction (4) requires the activation of dihydrogen and formation of O-H bonds. While Pd(111) terraces readily activate H<sub>2</sub> and bind the resulting H atoms favorably with  $\Delta E = -0.91$  eV for dissociative adsorption, In(001) terraces are hardly capable of activating H<sub>2</sub>. The activation barrier for H<sub>2</sub> dissociation on In(001) is  $E_a = 1.58$  eV and the step is endothermic by  $\Delta E = 1.33$  eV. Similar results are obtained for 1 ML In on Pd(111) ( $E_a = 1.51$  eV,  $\Delta E = 1.20$  eV). Therefore, a plausible mechanism for O\* removal from In sites would invoke the bifunctional nature of the In-on-Pd NPs, where Pd can supply H\* atoms to In ensembles to keep them reduced.

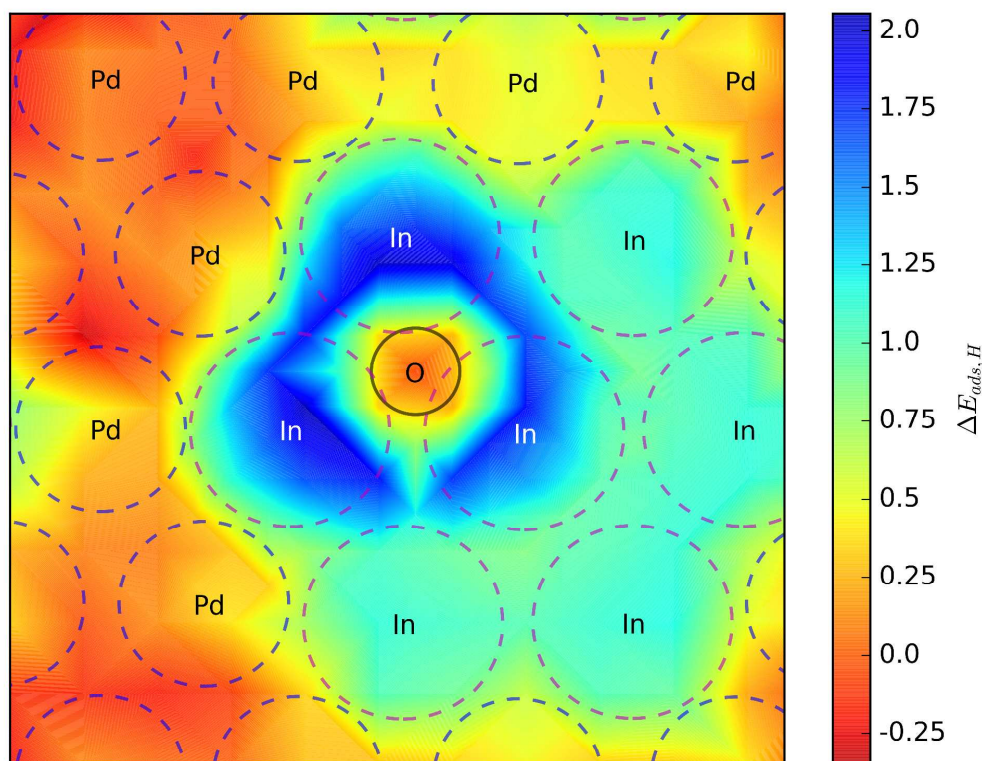


**Figure 10.** Potential energy contour map for H\* binding on a static 7-atom In ensemble with O\* in a In 3-fold site (In<sub>3</sub>-O). The dashed and solid circles outline the position of metal atoms and adsorbed oxygen, respectively.

1  
2  
3  
4 We first probed H\* binding on a static 7-atom In ensemble with O\* in a In 3-fold site  
5 (In<sub>3</sub>-O, Figure 10). The red color over the In<sub>3</sub>-O position corresponds to the formation of a strong  
6 O-H bond and the formation of an In<sub>3</sub>-OH species. On the free In sites (cyan color) hydrogen  
7 binds over 1 eV more weakly than on Pd sites. Access to the In<sub>3</sub>-O species was prohibited by  
8 strong repulsion when H\* is located above these In sites (blue color). The qualitative  
9 interpretation of this contour map is consistent with difficult reduction of large In clusters caused  
10 by limited availability of H\* near In<sub>3</sub>-O sites. Although Figure 9 provides a reasonable  
11 explanation why too much In is detrimental for nitrate reduction, it neglects surface relaxation  
12 effects and does not explain facile reduction of small In ensembles.

13  
14  
15  
16  
17  
18  
19  
20  
21  
22  
23  
24  
25 We next performed a detailed analysis for the case of a 4-atom In ensemble (25.0 sc%),  
26 which we identified as the approximate minimum threshold for fast nitrate reduction. In this case,  
27 the hydrogenation of In<sub>3</sub>-O to In<sub>3</sub>-OH with H\* originating from a 3-fold Pd site (Pd<sub>3</sub>-H) was  $\Delta E$   
28 = -0.79 eV exothermic and required a barrier of  $E_a = 0.79$  eV. The subsequent step to  
29 hydrogenate In<sub>3</sub>-OH with Pd<sub>3</sub>-H to form In-H<sub>2</sub>O had a similar barrier ( $E_a = 0.77$  eV) and was  
30 exothermic by  $\Delta E = -0.26$  eV. Both barriers are lower than the effective activation barrier for  
31 nitrate reduction ( $G_{TS}$ ) shown in Figure 8b and the assumption of rapid O\* removal appears valid  
32 for small In ensembles.

33  
34  
35  
36  
37  
38  
39  
40  
41  
42  
43 We note that the ensemble size effects discussed here cannot be captured in mean-field  
44 models, and more sophisticated kinetic Monte Carlo simulations with local coverage information  
45 would be required. From the modeling performed, however, we expect a strong promotional  
46 effect of In on nitrate reduction as long as the In ensembles do not exceed a critical size,  
47 consistent with the observed volcano-shape structure-activity plot based on In surface coverage.

### *In situ* XANES evidence for reduction and oxidation of In content

Figure 4d shows results from a room temperature *in situ* experiment in which a catalyst was exposed to a sequence of solutions of air- or 4% H<sub>2</sub>-saturated water. Contact of 40 sc% In-on-Pd NPs containing fully oxidized In with H<sub>2</sub> led to metallic In formation, and subsequent contact with air led to full In metal re-oxidation. A second cycle of H<sub>2</sub>/air contact confirmed redox cycling capability of the In metal. These results are evidence of In reducibility of our In-on-Pd NPs under *in situ* XAS testing conditions (room temperature, H<sub>2</sub> concentration estimated at ~31.2 μM). A fraction of the In content is likely to be in reduced form at the catalytic reaction conditions used, *i.e.*, at a higher H<sub>2</sub> aqueous concentration of ~390 μM, estimated from the 50/50 H<sub>2</sub>/CO<sub>2</sub> headspace composition). Interestingly, bulk In metal is expected to be thermodynamically unstable at room temperature at these pH and potential conditions in water (via Pourbaix analysis).<sup>84</sup>

We then carried a similar experiment in which a nitrate solution was used in place of air-saturated water. Contact of 40 sc% In-on-Pd NPs with air-saturated water ensured fully oxidized In, and subsequent contact with H<sub>2</sub>-containing water again led to metallic In formation. Exposure to a nitrate solution (100 ppm, also purged with dinitrogen gas) led to re-oxidation of the zerovalent In (Figure 11), strongly indicative of the In content being capable of redox cycling during the catalytic nitrate reduction process.

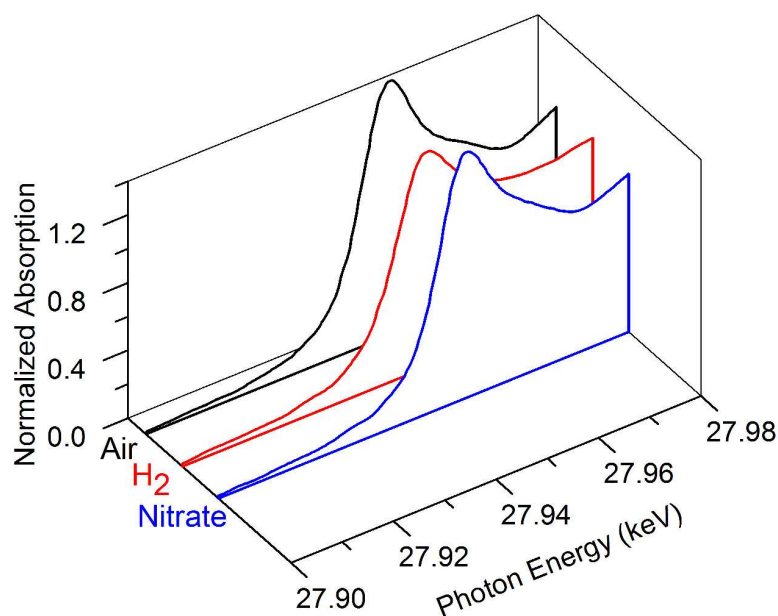


**Figure 11.** Room-temperature *in situ* XANES spectra (In K edge) of 40 sc% In-on-Pd NPs (a) in air-saturated water, (b) and then in 4% H<sub>2</sub>-saturated water, (c) followed by exposure to nitrate solution (100 ppm).

These experimental observations are congruent with a Bader charge analysis based on our electronic structure results. Using the 4-In atom ensemble as example (Figure 8e), Table 2 shows an increase of the average Bader charge on the 4 In atoms from *ca.* +0.5 |e<sup>-</sup>| for the reduced (clean) surface to *ca.* +0.85 |e<sup>-</sup>| for the oxidizing final state of N-O bond cleavage. The Bader charge increase for In atom #4 can be almost entirely attributed to its interaction with the abstracted O\* atom. The fractional Bader charge does not represent a formal oxidation state, but its increase is consistent with the XAS data showing an increase in the oxidation state of In during nitrate reduction.

**Table 2.** Bader charges in  $|e^-|$  for an In 4-mer within the Pd(111) top layer.

Atom Index	Pure Surface	IS	TS	FS
Atom #1	0.47	0.69	0.76	0.94
Atom #2	0.54	0.74	0.65	0.76
Atom #3	0.48	0.65	0.76	0.81
Atom #4	0.53	0.59	0.67	0.84

Based on the above experiments and simulations, the deposition of In can promote the reaction activity through two ways: (1) improve ability of the catalysts surface to adsorb nitrate ions, and (2) lower the activation energy for nitrate reduction.

Figure S4 shows the selectivity of the catalysts as a function of conversion. Regardless of composition, the measured selectivities to ammonium and nitrite were generally low ( $<2.5\%$ ), leading to a calculated selectivity to dinitrogen of 95% or better. A similar selectivity has been reported for a supported PdIn catalyst used in a fixed bed reactor, this was only true at relatively low nitrate conversions (30%); selectivity decreased to 70% at 95% nitrate conversions.<sup>85</sup> The ammonium selectivity increased slightly at higher conversions for the catalysts studied here (Figure S4b). Production of dinitrogen is thought to require the coupling of NO surface species<sup>42,86</sup> or by the reaction of NO with solution nitrite in an Eley-Rideal-like mechanism<sup>83</sup>, and it is natural that the selectivity to ammonium increases as the amount of available NO and nitrite decreases.

## Conclusions

We successfully synthesized a range of model In-on-Pd model catalysts, characterized them by TEM, XPS, and XANES, tested their catalytic activity toward aqueous phase nitrate reduction, and performed DFT and lumped kinetic modelling. *Ex situ* XPS showed the electronic state of In changed from the In<sup>0</sup> state to the In<sub>2</sub>O<sub>3</sub> state with increasing In coverage on the In-on-Pd NPs. *Ex situ* XANES showed that while the In was oxidized on the catalysts, exposure to mild reductive conditions (4% H<sub>2</sub> at 200 °C) partially reduced the In. *In situ* XANES further showed that exposure to 4% H<sub>2</sub>-saturated water was able to partially reduce In. While the monometallic analogues demonstrated no activity toward nitrate degradation, the optimum In-on-Pd NP catalyst had 40 at% of In, and a catalytic rate constant of 7.57 L g<sub>surface metal</sub><sup>-1</sup> min<sup>-1</sup>. DFT simulations and a lumped kinetic model showed that small In ensembles strongly favor nitrate reduction and can remain reduced via hydrogen spillover from adjacent Pd sites, while the reduction of large In ensembles is prohibitively difficult, which is in agreement with the experimentally observed In-dependent volcano-shaped activity. A Bader charge analysis indicated an increase in oxidation of In atoms during the nitrate reduction reaction and is consistent with *in situ* XANES experiments which showed oxidation of In in nitrate solution. Based on the experimental and computational evidence, we propose a mechanism in which In oxidatively adsorbs nitrate, while Pd activates hydrogen to further reduce formed nitrite and to regenerate In sites. These results suggest that bimetallic In-on-Pd NP catalysts are amenable for water nitrate pollution remediation and potentially other oxyanions.

## Supporting Information

Additional experimental details & DFT calculations, magic cluster calculations, mass transfer analysis

## Acknowledgement

M.S.W. acknowledges partial financial support from the NSF Nanosystems Engineering Research Center for Nanotechnology-Enabled Water Treatment (ERC-1449500). S.G. acknowledges financial support from the China Scholarship Council. S.K. and L.C.G. acknowledge financial support by the U.S. Department of Energy (DOE), Office of Science, Office of Basic Energy Sciences under award number DE-SC0011983. This research used resources of the National Energy Research Scientific Computing (NERSC) Center, a DOE Office of Science User Facility supported by the Office of Science of the U.S. DOE under Contract No. DE-AC02-05CH11231, and of the Center for Nanoscale Materials (CNM), supported by the U.S. DOE, Office of Science, Office of Basic Energy Sciences, under Contract No. DE-AC02-06CH11357. Additional computational resources were provided through the Extreme Science and Engineering Discovery Environment (XSEDE), which is supported by NSF (No. ACI5681053575) and HPC resources provided by the Texas Advanced Computing Center (TACC) at The University of Texas at Austin. We also acknowledge use of the Maxwell/Opuntia Cluster and the advanced support from the Center of Advanced Computing and Data Systems (CACDS) at the University of Houston facilitated under NSF-MRI Grant No. ACI-1531814. We thank Dr. C. Ayala for assistance in TEM characterization. S.K. sincerely acknowledges Dr. S. Wang for input in kinetic modeling.

## References

- (1) Wakida, F. T.; Lerner, D. N. *Water Research*, **2005**, *39*, 3–16.
- (2) Kapoor, A.; Viraraghavan, T. *J. Environ. Eng.* **1997**, *123*, 371–380.
- (3) Pintar, A.; Batista, J.; Levec, J.; Kajiuchi, T. *Appl. Catal. B Environ.* **1996**, *11*, 81–98.
- (4) Cantor, K. P. Drinking water and cancer. *Cancer Causes and Control*, **1997**, *8*, 292–308.

- 1
- 2
- 3
- 4 (5) Camargo, J. a.; Alonso, Á. *Environ. Int.* **2006**, *32*, 831–849.
- 5 (6) Nolan, J.; Weber, K. a. *Environ. Sci. Technol. Lett.* **2015**, *2*, 215–220.
- 6 (7) Oc, C. O. C.; Ioc, I. O. C. *Fed. Regist.* **2002**, *67*, 1811–1844.
- 7 (8) Council, T. H. E.; The, O. F.; Union, E. *Off. J. Eur. Communities.* **1998**, *L 330*, 32–54.
- 8 (9) Gorchev, H. G.; Ozolins, G. *WHO Chron.* **1984**, *38*, 104–108.
- 9
- 10
- 11 (10) Mulholland, P. J.; Helton, A. M.; Poole, G. C.; Hall, R. O.; Hamilton, S. K.; Peterson, B.  
12 J.; Tank, J. L.; Ashkenas, L. R.; Cooper, L. W.; Dahm, C. N.; Dodds, W. K.; Findlay, S. E.  
13 G.; Gregory, S. V.; Grimm, N. B.; Johnson, S. L.; McDowell, W. H.; Meyer, J. L.; Valett,  
14 H. M.; Webster, J. R.; Arango, C. P.; Beaulieu, J. J.; Bernot, M. J.; Burgin, A. J.;  
15 Crenshaw, C. L.; Johnson, L. T.; Niederlehner, B. R.; O'Brien, J. M.; Potter, J. D.;  
16 Sheibley, R. W.; Sobota, D. J.; Thomas, S. M. *Nature.* **2008**, *452*, 202–205.
- 17
- 18 (11) Shrimali, M.; Singh, K. *Environmental Pollution.* **2001**, *112*, 351–359.
- 19 (12) Ziv-El, M. C.; Rittmann, B. E. *Water Res.* **2009**, *43*, 173–181.
- 20 (13) Hu, Q.; Westerhoff, P.; Vermaas, W. *Appl. Environ. Microbiol.* **2000**, *66*, 133–139.
- 21 (14) Wong, M. S.; Alvarez, P. J. J.; Fang, Y. L.; Akçin, N.; Nutt, M. O.; Miller, J. T.; Heck, K.  
22 N. *J. Chem. Technol. Biotechnol.* **2009**, *84*, 158–166.
- 23 (15) Chaplin, B. P.; Reinhard, M.; Schneider, W. F.; Schüth, C.; Shapley, J. R.; Strathmann, T.  
24 J.; Werth, C. J. *Environ. Sci. Technol.* **2012**, *46*, 3655–3670.
- 25 (16) Pirkanniemi, K.; Sillanpää, M. *Chemosphere.* **2002**, *48*, 1047–1060.
- 26 (17) Ebbesen, S. D.; Mojet, B. L.; Lefferts, L. *J. Phys. Chem. C.* **2011**, *115*, 1186–1194.
- 27 (18) Chinthaginjala, J. K.; Lefferts, L. *Appl. Catal. B Environ.* **2010**, *101*, 144–149.
- 28 (19) Ebbesen, S. D.; Mojet, B. L.; Lefferts, L. *J. Catal.* **2008**, *256*, 15–23.
- 29 (20) Qian, H.; Zhao, Z.; Velazquez, J.; Pretzer, L. *Nanoscale.* **2014**, 358–364.
- 30 (21) Epron, F.; Gauthard, F.; Barbier, J. *J. Catal.* **2002**, *206*, 363–367.
- 31 (22) Matatov-Meytal, U.; Sheintuch, M. *Catal. Today.* **2005**, *102–103*, 121–127.
- 32 (23) Deganello, F.; Liotta, L. F.; Macaluso, a.; Venezia, a. M.; Deganello, G. *Appl. Catal. B*  
33 *Environ.* **2000**, *24*, 265–273.
- 34 (24) Palomares, A. E.; Franch, C.; Corma, A. *Catal. Today.* **2010**, *149*, 348–351.
- 35 (25) Hamid, S.; Kumar, M. A.; Lee, W. *Appl. Catal. B Environ.* **2016**, *187*, 37–46.
- 36 (26) Guy, K. a.; Xu, H.; Yang, J. C.; Werth, C. J.; Shapley, J. R. *J. Phys. Chem. C.* **2009**, *113*,  
37 8177–8185.
- 38 (27) Jung, J.; Bae, S.; Lee, W. *Appl. Catal. B Environ.* **2012**, *127*, 148–158.
- 39 (28) Prüsse, U.; Hähnlein, M.; Daum, J.; Vorlop, K.-D. *Catal. Today.* **2000**, *55*, 79–90.
- 40 (29) Chaplin, B. P.; Shapley, J. R.; Werth, C. J. *Catal. Letters.* **2009**, *130*, 56–62.
- 41 (30) Chaplin, B. P.; Shapley, J. R.; Werth, C. J. *Environ. Sci. Technol.* **2007**, *41*, 5491–5497.
- 42 (31) Marchesini, F. A.; Irusta, S.; Querini, C.; Miró, E. *Appl. Catal. A Gen.* **2008**, *348*, 60–70.
- 43 (32) Marchesini, F. A.; Irusta, S.; Querini, C.; Miró, E. *Catal. Commun.* **2008**, *9*, 1021–1026.
- 44
- 45
- 46
- 47
- 48
- 49
- 50
- 51
- 52
- 53
- 54
- 55
- 56
- 57
- 58
- 59
- 60

- 1  
2  
3 (33) Gao, Z.; Zhang, Y.; Li, D.; Werth, C. J.; Zhang, Y.; Zhou, X. *J. Hazard. Mater.* **2015**, *286*,  
4 425–431.  
5  
6 (34) Lemaigen, L.; Tong, C.; Begon, V.; Burch, R.; Chadwick, D. *Catal. Today.* **2002**, *75*,  
7 43–48.  
8  
9 (35) Zhao, Z.; Fang, Y. L.; Alvarez, P. J. J.; Wong, M. S. *Appl. Catal. B Environ.* **2013**, *140–*  
10 *141*, 468–477.  
11  
12 (36) Pretzer, L. A.; Song, H. J.; Fang, Y. L.; Zhao, Z.; Guo, N.; Wu, T.; Arslan, I.; Miller, J. T.;  
13 Wong, M. S. *J. Catal.* **2013**, *298*, 206–217.  
14  
15 (37) Zhou, K.; Wang, W.; Zhao, Z.; Luo, G.; Miller, J. T.; Wong, M. S.; Wei, F. *ACS Catal.*  
16 **2014**, *4*, 3112–3116.  
17  
18 (38) Kimberly N. Heck, Benjamin G. Janesko, Gustavo E. Scuseria, Naomi J. Halas, and M. S.  
19 W. *ACS Catal.* **2013**, *3*, 2430–2435.  
20  
21 (39) Zhao, Z.; Arentz, J.; Pretzer, L. a; Limpornpipat, P.; Clomburg, J. M.; Gonzalez, R.;  
22 Schweitzer, N.; Wu, T.; Miller, J. T.; Wong, M. *Chem. Sci.* **2014**, *5*, 3715–3728.  
23  
24 (40) Pretzer, L. A.; Heck, K. N.; Kim, S. S.; Fang, Y. L.; Zhao, Z.; Guo, N.; Wu, T.; Miller, J.  
25 T.; Wong, M. S. *Catal. Today.* **2016**, *264*, 31–36.  
26  
27 (41) Nutt, M. O.; Heck, K. N.; Alvarez, P.; Wong, M. S. *Appl. Catal. B Environ.* **2006**, *69*,  
28 115–125.  
29  
30 (42) Zhang, R.; Shuai, D.; Guy, K. a.; Shapley, J. R.; Strathmann, T. J.; Werth, C. J.  
31 *ChemCatChem.* **2013**, *5*, 313–321.  
32  
33 (43) Nelson, R. C.; Miller, J. T. *Catal. Sci. Technol.* **2012**, *2*, 461–470.  
34  
35 (44) Fang, Y. L.; Heck, K. N.; Alvarez, P. J. J.; Wong, M. S. *ACS Catal.* **2011**, *1*, 128–138.  
36  
37 (45) Boltz, D. F. *Colometric determination of nonmetals.*; John Wiley: New York. **1978**, 216–  
38 239.  
39  
40 (46) Green, L. C.; Wagner, D. A.; Glogowski, J.; Skipper, P. L.; Wishnok, J. S.; Tannenbaum,  
41 S. R. *Anal. Biochem.* **1982**, *126*, 131–138.  
42  
43 (47) Hohenberg, P.; Kohn, W. *Phys. Rev.* **1964**, *136*, B864–B871.  
44  
45 (48) Kresse, G.; Hafner, J. *Phys. Rev. B.* **1993**, *47*, 558–561.  
46  
47 (49) Kresse, G.; Hafner, J. *Phys. Rev. B.* **1994**, *49*, 14251–14269.  
48  
49 (50) Kresse, G.; Furthmüller, J. *Comput. Mater. Sci.* **1996**, *6*, 15–50.  
50  
51 (51) Kresse, G. *Phys. Rev. B.* **1996**, *54*, 11169–11186.  
52  
53 (52) Perdew, J. P.; Burke, K.; Ernzerhof, M. *Phys. Rev. Lett.* **1996**, *77*, 3865–3868.  
54  
55 (53) Hammer, B.; Hansen, L.; Nørskov, J. *Phys. Rev. B.* **1999**, *59*, 7413–7421.  
56  
57 (54) Blöchl, P. E. *Phys. Rev. B.* **1994**, *50*, 17953–17979.  
58  
59 (55) Kresse, G. *Phys. Rev. B.* **1999**, *59*, 1758–1775.  
60  
61 (56) Gillan, M. J. *J. Phys. Condens. Matter.* **1989**, *1*, 689–711.  
62  
63 (57) Tang, W.; Sanville, E.; Henkelman, G. *J. Phys. Condens. Matter.* **2009**, *21*, 84204–84204.

- 1  
2  
3 (58) Sanville, E.; Kenny, S. D.; Smith, R.; Henkelman, G. *J. Comput. Chem.* **2007**, *28*, 899–  
4 908.  
5  
6 (59) Henkelman, G.; Arnaldsson, A.; Jónsson, H. *Comput. Mater. Sci.* **2006**, *36*, 354–360.  
7  
8 (60) Yu, M.; Trinkle, D. R. *J. Chem. Phys.* **2011**, *134*, 1–8.  
9  
10 (61) Bengtsson, L. *Phys. Rev. B.* **1999**, *59*, 12301–12304.  
11  
12 (62) Pack, J.; Monkhorst, H. *Phys. Rev. B.* **1977**, *16*, 1748–1749.  
13  
14 (63) Bergerhoff, G.; Hundt, R.; Sievers, R.; Brown, I. D. *J. Chem. Inf. Model.* **1983**, *23*, 66–69.  
15  
16 (64) Moshopoulou, E. G.; Ibberson, R. M.; Sarrao, J. L.; Thompson, J. D.; Fisk, Z.  
17 *Electrochem. Solid-State Lett.* **2006**, *9*, 173–189.  
18  
19 (65) Lide, D. R. *Ionization potentials of atoms and atomic ions.* **1992**, 10-211.  
20  
21 (66) Berkowitz, J. *J. Chem. Phys.* **1971**, *55*, 2724-2733.  
22  
23 (67) Jónsson, H.; Mills, G.; Jacobsen, K. W. *Class. Quantum Dyn. Condens. Phase Simulations*  
24 *- Proc. Int. Sch. Phys.* **1998**, 385–404.  
25  
26 (68) Henkelman, G.; Jónsson, H. *J. Chem. Phys.* **2000**, *113*, 9978-9985.  
27  
28 (69) Henkelman, G.; Uberuaga, B. P.; Jónsson, H. *J. Chem. Phys.* **2000**, *113*, 9901-9904.  
29  
30 (70) Sheppard, D.; Terrell, R.; Henkelman, G. *J. Chem. Phys.* **2008**, *128*, 134106-134106.  
31  
32 (71) Sheppard, D.; Henkelman, G. *J. Comput. Chem.* **2011**, *32*, 1769–1771.  
33  
34 (72) Sheppard, D.; Xiao, P.; Chemelewski, W.; Johnson, D. D.; Henkelman, G. *J. Chem. Phys.*  
35 **2012**, *136*, 74103-74103.  
36  
37 (73) Henkelman, G.; Jónsson, H. *J. Chem. Phys.* **1999**, *111*, 7010–7022.  
38  
39 (74) Heyden, A.; Bell, A. T.; Keil, F. J. *J. Chem. Phys.* **2005**, *123*, 224101-224101.  
40  
41 (75) Kästner, J.; Sherwood, P. *J. Chem. Phys.* **2008**, *128*, 14106-14106.  
42  
43 (76) Xiao, P.; Sheppard, D.; Rogal, J.; Henkelman, G. *J. Chem. Phys.* **2014**, *140*, 214110-  
44 214110.  
45  
46 (77) Alexander V. Naumkin, Anna Kraut-Vass, Stephen W. Gaarenstroom, and C. J. P. NIST  
47 X-ray Photoelectron Spectroscopy Database, Version 4.1  
48 [http://srdata.nist.gov/xps/EngElmSrchQuery.aspx?EType=PE&CSOpt=Retri\\_ex\\_dat&Elm=In](http://srdata.nist.gov/xps/EngElmSrchQuery.aspx?EType=PE&CSOpt=Retri_ex_dat&Elm=In) (accessed Jan 29, 2016).  
49  
50 (78) Toshima, N.; Harada, M.; Yonezawa, T.; Kushibashi, K.; Asakurat, K. *J. Phys. Chem.*  
51 **1991**, *95*, 7448–7453.  
52  
53 (79) Bradley, J. S.; Via, G. H.; Bonneviot, L.; Hill, E. W. *Chem. Mater.* **1996**, *8*, 1895–1903.  
54  
55 (80) Wu, Z.; Wegener, E. C.; Tseng, H.-T.; Gallagher, J. R.; Harris, J. W.; Diaz, R. E.; Ren, Y.;  
56 Ribeiro, F. H.; Miller, J. T. *Catal. Sci. Technol.* **2016**, *6*, 6965–6976.  
57  
58 (81) Chinthajjala, J. K.; Lefferts, L. *Appl. Catal. B Environ.* **2010**, *101*, 144–149.  
59  
60 (82) Pintar, A.; Bereie, G. Levec, J. **1998**, *44*, 2280-2292.  
61  
62 (83) Shin, H.; Jung, S.; Bae, S.; Lee, W.; Kim, H. *Environ. Sci. Technol.* **2014**, *48*, 12768–  
63 12774.

- 1  
2  
3 (84) Parsons, R. *J. Electroanal. Chem. Interfac.* **1967**, *13*, 471-471.  
4  
5 (85) Mendow, G.; Marchesini, F. a.; Mir, E. E.; Querini, C. a. *Ind. Eng. Chem. Res.* **2011**, *50*,  
6 1911–1920.  
7  
8 (86) Zhao, Y.; Koteswara Rao, N.; Lefferts, L. *J. Catal.* **2016**, *337*, 102–110.  
9  
10  
11  
12  
13  
14  
15  
16  
17  
18  
19  
20  
21  
22  
23  
24  
25  
26  
27  
28  
29  
30  
31  
32  
33  
34  
35  
36  
37  
38  
39  
40  
41  
42  
43  
44  
45  
46  
47  
48  
49  
50  
51  
52  
53  
54  
55  
56  
57  
58  
59  
60

## TOC Graphic

